Eur. Phys. J. E (2012) **35**: 58
DOI 10.1140/epje/i2012-12058-1

THE EUROPEAN PHYSICAL JOURNAL E

Colloquium

New perspectives in turbulent Rayleigh-Bénard convection

F. Chillà[1,a] and J. Schumacher[2,b]

[1] Laboratoire de Physique, École Normale Supérieure de Lyon, 46 Allée d'Italie, F-69364 Lyon, France
[2] Institut für Thermo- und Fluiddynamik, Postfach 100565, Technische Universität Ilmenau, D-98684 Ilmenau, Germany

Received 15 May 2012 and Received in final form 15 June 2012
Published online: 13 July 2012

Abstract. Recent experimental, numerical and theoretical advances in turbulent Rayleigh-Bénard convection are presented. Particular emphasis is given to the physics and structure of the thermal and velocity boundary layers which play a key role for the better understanding of the turbulent transport of heat and momentum in convection at high and very high Rayleigh numbers. We also discuss important extensions of Rayleigh-Bénard convection such as non-Oberbeck-Boussinesq effects and convection with phase changes.

1 Introduction

Turbulent convection is an omnipresent process in Nature and technology. Many turbulent flows are driven and sustained by temperature differences such as convection inside stars and planets [1,2], atmospheric motion [3,4] or circulation in the ocean [5]. Convection plays an important role in heat exchangers and passive cooling devices for electronic equipments and computer chips [6]. Convective motion determines also the quality of the indoor air circulation in rooms and passenger cabins [7]. In most cases the turbulent convective motion is coupled to other physical processes such as rotation of the frame of reference, radiative transfer, phase changes and chemical reactions. In other situations the convection is influenced by electromagnetic fields, by particles dispersed in the fluid or it is constrained by the porosity of the medium in which it evolves.

The simplest paradigm for all the cases above is the so-called Rayleigh-Bénard convection [8]. An infinitely extended fluid layer of height H is heated from below and cooled from above. The horizontal boundary planes at the top and at the bottom are held at constant temperatures, $T_{\rm top}$ (at $z = H$) and $T_{\rm bottom}$ (at $z = 0$), respectively, such that $\Delta T = T_{\rm bottom} - T_{\rm top} > 0$ (see fig. 1). Alternatively, one can prescribe a constant flux of heat across both boundaries by fixing $\mathrm{d}T/\mathrm{d}z$. The driving force for thermal convection is the buoyancy. When a fluid parcel becomes warmer it expands and its mass density decreases. Suppose that the fluid parcel is in a gravitational field and heating is applied from below such that cold, dense fluid is on top of warmer, lighter fluid. Then a parcel will rise when the buoyancy force can overcome viscous drag and thermal diffusion. This physics can be summarized in two dimensionless parameters, the Rayleigh number Ra and the Prandtl number Pr which are given by

$$Ra = \frac{g\alpha\Delta T H^3}{\nu\kappa}\,, \qquad Pr = \frac{\nu}{\kappa}\,, \qquad \Gamma = \frac{L}{H}\,. \tag{1}$$

The third parameter in (1) is the aspect ratio Γ where L denotes a characteristic horizontal scale such as the diameter of a cylindrical convection cell. Quantity g is the gravity acceleration and α the thermal expansion coefficient. The Rayleigh number quantifies the competition of upward motion of a fluid parcel due to positive buoyancy in comparison to drag and diffusion. The Prandtl number compares the kinematic viscosity ν and thermal diffusivity κ of the fluid. In table 1 we summarize a few examples of turbulent convection and list the corresponding estimates for the Rayleigh and Prandtl numbers as well as the involved scales. The examples show that a wide range of parameters is covered which puts a challenge on describing the convective turbulence. We also indicate that in most cases convective turbulence is accompanied by other physical processes as stated already above.

One of the key questions is that of the turbulent transport mechanisms of heat and momentum across the layer, in other words, how is the turbulent fluid carrying heat and momentum from the bottom to the top [14,15]. Since the fluid is confined between rigid or/and impermeable walls boundary layers of the temperature and velocity fields will form in the vicinity. The deeper understanding of the transport mechanisms requires thus a deeper understanding of the physics in these boundary layers. As being the case in many other wall-bounded flows, the fluid dynamics is tightly connected to near-wall coherent structures. Understanding the boundary layer dynamics itself

[a] e-mail: fchilla@ens-lyon.fr
[b] e-mail: joerg.schumacher@tu-ilmenau.de

Table 1. Examples for convection and estimates of the Rayleigh and Prandtl numbers, Ra and Pr. We also list a typical vertical scale H of the convection process and a typical aspect ratio $\Gamma = L/H$ both of which should be understood as order-of-magnitude estimates. In case of the Earth mantle and solar convection the circumferences at mid height have been taken for L.

	Ra	Pr	H	Γ	Remark
Mantle convection [9]	10^7–10^9	10^{23}	700 km	54	Creeping flow limit with phase transitions
Deep oceanic convection [10]	10^{24}–10^{27}	7	1–4 km	10^2–10^3	Ra based on buoyancy flux
Processor cooling device	10^6	0.7	1–10 cm	1	Complex geometry effects
Indoor ventilation	10^8–10^{10}	0.7	1–10 m	1–10	Mostly mixed convection
Shallow moist convection [11]	10^{18}	0.7	2 km	10^2	Vapor and water; Conditionally unstable
Deep moist convection	10^{22}	0.7	10 km	10^2	Vapor, water and ice; Anelastic limit
Solar convection zone [12,13]	10^{20}–10^{24}	10^{-7}–10^{-3}	2×10^5 km	10	Highly compressible

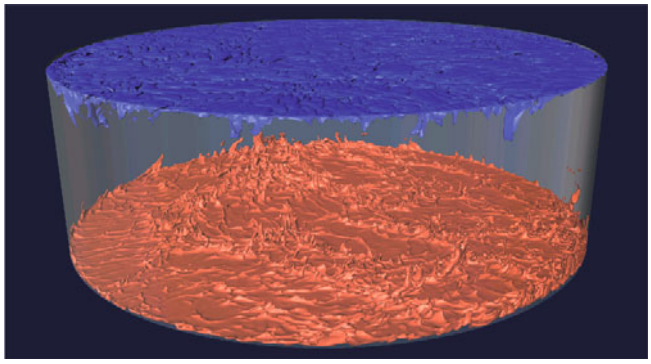

Fig. 1. The typical Rayleigh-Bénard convection setup as a cylindrical cell. Two isosurfaces of the temperature are shown: hot at the bottom for $T/\Delta T = 0.7$ in red, cold at the top for $T/\Delta T = 0.3$ in blue. Parameters are here: $Ra = 10^9$, $Pr = 0.7$ and $\Gamma = 3$ (see [26,27] for the corresponding simulations).

thus requires to understand their formation and their statistical weight for the global transport.

In this colloquium paper we want to review some of the recent developments in high-Rayleigh number convection. Significant progress in our understanding of turbulent convection has been obtained in the last years by both, experimental and numerical studies of turbulent convection. We want to summarize these results, discuss some possible extensions towards more complex physical situations and will give an outlook to some possible future directions in this vital field of fluid dynamics research. Since we cannot cover all aspects in detail, we want to point the interested reader to other recent reviews of turbulent convection such as the ones by Ahlers *et al.* [16] on heat transport and large-scale mechanisms, the one by Lohse and Xia [17] on small-scale properties in turbulent Rayleigh-Bénard convection. Further recent studies on our subject can be found in a focus issue [18]. The vast variety of convective processes makes it impossible to discuss all of them. We will restrict our following discussion therefore to the three-dimensional (3D) non-rotating convection case.

Section 2 summarizes the equations of motion, the dimensionless parameters and some basic relations that are a consequence of the equations. In sect. 3, we discuss existing scaling theories for the global heat and momentum transfer, in particular for the so-called ultimate regime at very high Rayleigh numbers. Section 4 gives a short overview over experimental devices and numerical methods. In sect. 5, we discuss studies up to Rayleigh number $Ra \sim 10^{12}$ with a particular emphasis on structures in the boundaries and the large-scale circulation. Section 6 summarizes very-high-Rayleigh number experiments and DNS beyond $Ra \sim 10^{12}$ and is followed by extensions of the classical Rayleigh-Bénard convection in sect. 7 and an outlook in sect. 8.

2 Oberbeck-Boussinesq model

The most general starting point for the equations of motion in convective turbulence is to take the full set of compressible flow equations containing the balances of mass, momentum and energy. In the balance of the momentum density ρu_i, a volume force density ρg_i appears with gravity acceleration vector $g_i = (0, 0, -g)$. The mass density $\rho(T, p)$ is connected to the pressure p and the temperature T by an equation of state, usually the one for an ideal gas which is given by (R is the specific gas constant)

$$p = R\rho T \qquad \text{and thus} \qquad \frac{1}{\rho}\frac{\mathrm{d}\rho}{\mathrm{d}t} = \frac{1}{p}\frac{\mathrm{d}p}{\mathrm{d}t} - \frac{1}{T}\frac{\mathrm{d}T}{\mathrm{d}t}\,. \quad (2)$$

In the following, we simplify ρg_i in two steps as being relevant for convective motion in planetary atmospheres where the fluid motion is considered to be quasi-adiabatic [19]. Further discussion is found in [20,21]. The continuity equation for the mass density ρ is given by

$$\frac{1}{\rho}\frac{\mathrm{d}\rho}{\mathrm{d}t} = -\frac{\partial u_i}{\partial x_i} \qquad \text{and thus} \qquad \frac{1}{\rho}\frac{\mathrm{d}\rho}{\mathrm{d}t} = \frac{c_v}{c_p}\frac{\mathrm{d}}{\mathrm{d}t}\ln p, \quad (3)$$

follows when (2) and the adiabatic form of the first law of thermodynamics are used [19]. Here, c_p and c_v are the specific heats at constant pressure and volume, respectively, and $c_p = c_v + R$. The time derivatives in (3) should be understood as a substantial derivative. Re-expressed in characteristic scales and amplitudes this results to (dimensionless quantities with a tilde)

$$-\frac{\partial \tilde{u}_i}{\partial \tilde{x}_i} = \frac{u_0^2}{c_s^2}\left[\frac{\partial}{\partial \tilde{t}} + \tilde{\mathbf{u}}_h \cdot \tilde{\nabla}_h\right]\ln \tilde{p} + \frac{c_v H}{c_p L_z}\tilde{u}_z \frac{\partial \ln \tilde{p}}{\partial \tilde{z}}\,, \quad (4)$$

where $c_s = \sqrt{c_p RT/c_v}$ is the adiabatic velocity of sound in an ideal gas. Index h in (4) stands for horizontal terms in (x, y).

The first level of simplification is now as follows. If the characteristic velocity of the convective turbulence is much smaller than the speed of sound then the first term on the right hand side can be neglected. This is the so-called *anelastic approximation* of thermal convection. The mass density becomes time-independent and the continuity equation contains the vertical advection of mass only [22]. The last term of eq. (4) contains a ratio of scales, H the vertical scale of convection and L_z the outer scale of pressure variation (in atmospheric context, the height of the atmosphere). If $H \sim L_z$ then eq. (4) can be rewritten with (3) to

$$-\frac{\partial \tilde{u}_i}{\partial \tilde{x}_i} = \frac{1}{\tilde{\rho}} \tilde{u}_z \frac{\partial \tilde{\rho}}{\partial \tilde{z}} \qquad \text{and thus} \qquad \frac{\partial}{\partial x_i}(\rho_{\rm ref} u_i) \approx 0, \quad (5)$$

where $\rho_{\rm ref}$ is a reference mass density. In several astrophysical and atmospheric convection flows this approximation has to be taken into account (see also table 1).

The second level is obtained if additionally $H \ll L_z$ holds in (4). The convection flow becomes incompressible and thus the *Oberbeck-Boussinesq (OB) approximation* [23,24] can be used. In this case all material parameters of the fluid are assumed to be independent of temperature and pressure, except the mass density which varies at first order in the buoyancy term (see also ref. [25] for a detailed discussion). Physically this means that the height of the convection layer is small enough such that small variations about a hydrostatic equilibrium have to be included only. As a consequence $\rho(T,p) = \rho(T)$ and

$$\begin{aligned}\rho(T) &= \rho(T_{\rm ref}) + \left.\frac{\partial \rho}{\partial T}\right|_{T=T_{\rm ref}} (T - T_{\rm ref}) + \dots \\ &= \rho_{\rm ref} - \frac{\rho}{V}\left.\frac{\partial V}{\partial T}\right|_p (T - T_{\rm ref}) + \dots \\ &\simeq \rho_{\rm ref}\big[1 - \alpha(T - T_{\rm ref})\big], \end{aligned} \quad (6)$$

with $\alpha = (1/V)\partial V/\partial T|_p = -(1/\rho)\partial\rho/\partial T|_p$ being the thermal expansion coefficient at constant pressure. The first term of (6) contributes to the hydrostatic equilibrium profile which is determined by $-\partial p_{\rm ref}/\partial x_i + \rho_{\rm ref} g_i = 0$. We see that the OB approximation is tightly coupled to an incompressible flow and the three-dimensional Boussinesq equations in Cartesian coordinates are given by

$$\frac{\partial u_i}{\partial t} + u_j \frac{\partial u_i}{\partial x_j} = -\frac{1}{\rho_0}\frac{\partial p'}{\partial x_i} + \nu \frac{\partial^2 u_i}{\partial x_j^2} + \alpha g (T - T_{\rm ref})\delta_{iz}, \quad (7)$$

$$\frac{\partial u_i}{\partial x_i} = 0, \quad (8)$$

$$\frac{\partial T}{\partial t} + u_j \frac{\partial T}{\partial x_j} = \kappa \frac{\partial^2 T}{\partial x_j^2}, \quad (9)$$

where $i,j = x,y,z$. Here, $p'(x,y,z,t)$ is the pressure variation about the hydrostatic equilibrium profile, $u_i(x,y,z,t)$ the velocity field, $T(x,y,z,t)$ the total temperature field. Thermal diffusivity $\kappa = k/(\rho_{\rm ref} c_p)$ contains the thermal conductivity k. The last term on the right hand side of (7) is also known as the buoyancy B.

Characteristic amplitudes can be composed out of the scales and material constants. These are for example the so called free-fall velocity $U_f = \sqrt{g\alpha\Delta T H}$ or a diffusive velocity $U_d = \kappa/H$. Characteristic time scales follow to a free-fall time $T_f = H/U_f$ and $T_d = H/U_d = H^2/\kappa$, respectively. This allows to derive a few relations such as $RaPr = U_f^2/U_d^2$ or $Ra/Pr = U_f^2 H^2/\nu^2 = Re_f^2$ where Re_f is a Reynolds number based on free-fall velocity.

In response to parameters Ra, Pr and Γ, the turbulent transport of heat and momentum is quantified by the Nusselt and Reynolds numbers, Nu and Re, respectively. They are given by

$$Nu = \frac{\langle u_z T\rangle_{A,t} - \kappa \dfrac{\partial \langle T\rangle_{A,t}}{\partial z}}{\kappa \Delta T/H}, \qquad Re = \frac{UH}{\nu}. \quad (10)$$

The average $\langle\cdot\rangle_{A,t}$ is taken over planes at fixed z and time. Velocity U can be U_f or a root-mean-square velocity. The two contributions in the numerator of (10) are due to the convective and diffusive heat currents which will be denoted as $J_c(\mathbf{x},t) = u_z T$ and $J_d(\mathbf{x},t) = -\kappa\partial_z T$. In the absence of fluid motion, heat can be carried by diffusion only across the fluid layer which will correspond with $Nu = 1$. With the Nusselt number at the bottom (top) plate $z = 0$ ($z = H$), which consists of a diffusive contribution only, one can derive an expression for the thermal boundary layer thickness in turbulent convection. If one assumes that $\partial\langle T\rangle_{A,t}/\partial z|_{z=0,H} = -\Delta T/(2\delta_T)$ the boundary layer thickness is given by

$$\delta_T = \frac{H}{2Nu}. \quad (11)$$

The decomposition of the temperature T into mean and fluctuations,

$$T(\mathbf{x},t) = \langle T(z)\rangle_{A,t} + \theta(\mathbf{x},t), \quad (12)$$

where $\langle\theta(\mathbf{x},t)\rangle_{A,t} = 0$, will be used throughout the text.

3 Scaling theories of turbulent transport

In the following we briefly summarize some predictions from scaling theories for the turbulent heat and momentum transport. Emphasis is given on which physical assumptions and concepts enter these theories rather than which particular scaling $Nu(Ra,Pr)$ and $Re(Ra,Pr)$ follows. A more detailed discussion is found in refs. [14] and [16] as mentioned already in the introduction. The latter reference contains a table in which all the scaling laws $Nu \sim Ra^\beta$ and $Re \sim Ra^\gamma$ are summarized and the historical development is outlined. We will focus here to the most prominent cases.

3.1 Scaling theory by Malkus

One of the oldest theoretical models that aims at predicting the Nusselt number as a function of the Rayleigh

number goes back to Malkus [28] based on his own laboratory experiments [29]. He suggested that the marginal stability argument, which is used to derive the onset of thermal convection, works also in the turbulent case where a mean flow configuration provides the "basic" state for which a perturbation analysis is applied. From this ansatz he derived a scaling law of

$$Nu \sim Ra^{1/3}. \tag{13}$$

Two aspects are worth to be mentioned. First, an exponent of 1/3 follows also if the heat transport is assumed to be independent of height, in other words, that the two boundary layers at the top and the bottom do not communicate. Second, Malkus discusses in his work also that for larger Rayleigh numbers a transition from a laminar to a turbulent boundary layer should be present [28].

3.2 Exact relationships

Two scaling theories of turbulent convection which we will outline now start with exact relations that can be derived from the Boussinesq equations. A central role is played by the kinetic energy dissipation rate $\epsilon(\mathbf{x},t)$ and the thermal dissipation rate $\epsilon_T(\mathbf{x},t)$ which are given by

$$\epsilon(\mathbf{x},t) = \frac{\nu}{2}\sum_{i,j}\left(\frac{\partial u_i}{\partial x_j}+\frac{\partial u_j}{\partial x_i}\right)^2, \tag{14}$$

$$\epsilon_T(\mathbf{x},t) = \kappa\sum_{i}\left(\frac{\partial T}{\partial x_i}\right)^2. \tag{15}$$

The balances of the turbulent kinetic energy as following from (7) and of the thermal variance as resulting from (9) give the following two exact relations:

$$\langle\epsilon\rangle = \frac{\nu^3}{H^4}(Nu-1)RaPr^{-2}, \tag{16}$$

$$\langle\epsilon_T\rangle = \kappa\frac{\Delta T^2}{H^2}Nu, \tag{17}$$

where the brackets $\langle\cdot\rangle$ denote a statistical ensemble average. The following scaling theories are based on specific assumptions for the physics in the thin thermal and velocity boundary layers. This also means that both rely on the existence of a large-scale wind that blows steadily across both plates in the turbulent convection cell. Such a large-scale circulation has been studied in many laboratory experiments and DNS up to $Ra \sim 10^{12}$ and will be discussed further below.

3.3 Scaling theory by Shraiman and Siggia

Shraiman and Siggia assume the existence of a turbulent boundary layer [14,30]. The following mean downstream velocity profile is consequently assumed:

$$\langle u_x(z)\rangle = \begin{cases} u_\tau z/z_\tau, & \text{if } z \le (7-12)z_\tau, \\ u_\tau\left[\frac{1}{\overline{\kappa}}\ln(z/z_\tau)+B\right], & \text{if } z > (7-12)z_\tau, \end{cases} \tag{18}$$

with the von Kármán constant $\overline{\kappa} = 0.4$; B depends on the shear flow geometry and was set to 5 in [14]. Here, $u_\tau = \sqrt{\tau_w/\rho_0}$ is the friction velocity with the wall shear stress which is defined as $\tau_w = \rho_0\nu\partial u_x/\partial z|_{z=0} = \rho_0\nu S$. The quantity $z_\tau = \nu/u_\tau$ denotes the corresponding viscous length scale. For $Pr > 1$ the thermal boundary layer will be nested in the velocity boundary layer and thus boundary layer equation to be solved close to the wall is (see eq. (18) for the viscous buffer layer)

$$u_x(z)\frac{\partial T}{\partial x} = Sz\frac{\partial T}{\partial x} \simeq \kappa\frac{\partial^2 T}{\partial z^2}, \tag{19}$$

which transforms to $f'(\eta)+(\eta^2/3)f(\eta)=0$ with a new similarity variable $\eta = [z^3S/(\kappa x)]^{1/3}$ and $f(\eta) = \tilde{T}'(\eta)$ with $\tilde{T} = T/\Delta T$. As a result one gets

$$\tilde{T}(\eta) = \tilde{T}(0) - C\int_0^\eta \exp(-\xi^3/9)\mathrm{d}\xi. \tag{20}$$

Consequently, the Nusselt number can be expressed as

$$Nu = \tilde{T}'(\eta=0) \sim \tilde{S}^{1/3} \sim \left(\frac{\tilde{u}_\tau^2}{Pr}\right)^{1/3}. \tag{21}$$

These relations follow when the OB equations (7)–(9) are nondimensionalzed by H and κ. Equation (16) simplifies then to $\langle(\tilde{\nabla}\tilde{\mathbf{u}})^2\rangle = NuRa$ for $Nu \gg 1$. Furthermore, the kinetic energy dissipation rate was estimated in [30] with

$$Pr\langle(\tilde{\nabla}\tilde{\mathbf{u}})^2\rangle \sim 100\tilde{u}_\tau^3. \tag{22}$$

If we plug (21) and (22) together and eliminate $\tilde{u}_\tau$ then

$$Nu \simeq 0.27Pr^{-1/7}Ra^{2/7}, \tag{23}$$

follows for the global heat transport and

$$Re \simeq 0.14Pr^{-5/7}Ra^{3/7}\left[\overline{\kappa}^{-1}\ln(Re)+B\right], \tag{24}$$

for the global momentum transport follows in a similar way. Equation (24) contains thus logarithmic corrections.

3.4 Scaling theory by Grossmann and Lohse

The central idea of the theory by Grossmann and Lohse [15] is to split both mean dissipation rates into two contributions each, one from the bulk (Bu) and one from the boundary layers (BL) so that

$$\langle\epsilon\rangle_{V,t} = \langle\epsilon\rangle_{Bu,t} + \langle\epsilon\rangle_{BL,t}, \tag{25}$$

$$\langle\epsilon_T\rangle_{V,t} = \langle\epsilon_T\rangle_{Bu,t} + \langle\epsilon_T\rangle_{BL,t}. \tag{26}$$

Note that the average $\langle\cdot\rangle_{Bu,t}$ contains bulk volume fractions v_{Bu} and v'_{Bu} for the viscous and thermal boundary layers, respectively. For high Ra both are practically one. Similarly, $\langle\cdot\rangle_{BL,t}$ contains the boundary layer volume fractions $v_{BL} = \delta_v/H$ and $v'_{BL} = \delta_T/H$ (see also eqs. (28)

to (32)). For the velocity (or viscous) BL a Blasius-type layer [31] is assumed with a thickness of

$$\delta_v = a\frac{H}{\sqrt{Re}}\,, \tag{27}$$

where the length L of the plate is set to be about the height H (or $\Gamma = 1$). The prefactor a is obtained by match with a record of experimental results as discussed in [15, 16]. The original Blasius solution for a two-dimensional laminar flow over a flat plate gives $a = 5$ [31].

Equations (25) and (26) together with (16) and (17) and the knowledge of the BL thicknesses set the stage to derive scaling relations in four basic regimes of turbulent convection. They consist of the four possible combinations of bulk and BL-dominated thermal and kinetic energy dissipation rates. These regimes cover different parts of the parameter plane that is spanned by the Rayleigh and Prandtl number (see fig. 3 in [16]). The four contributions to the dissipation can be estimated as follows:

$$\langle\epsilon\rangle_{Bu,t} \sim \frac{U^3}{H} \sim \frac{\nu^3}{H^4}Re^3, \tag{28}$$

$$\langle\epsilon\rangle_{BL,t} \sim \nu\frac{U^2}{\delta_v^2}\frac{\delta_v}{H} \sim \frac{\nu^3}{H^4}Re^{5/2}, \tag{29}$$

$$\langle\epsilon_T\rangle_{Bu,t} \sim \frac{U(\Delta T)^2}{H} \sim \kappa\frac{(\Delta T)^2}{H^2}PrRe, \tag{30}$$

$$\langle\epsilon_T\rangle_{BL,t}^{Pr\leq 1} \sim \kappa\frac{(\Delta T)^2}{\delta_T^2}\frac{\delta_T}{H} \sim \kappa\frac{(\Delta T)^2}{H^2}Pr^{1/2}Re^{1/2}, \tag{31}$$

$$\langle\epsilon_T\rangle_{BL,t}^{Pr\gg 1} \sim \kappa\frac{(\Delta T)^2}{\delta_T^2}\frac{\delta_T}{H} \sim \kappa\frac{(\Delta T)^2}{H^2}Pr^{1/3}Re^{1/2}. \tag{32}$$

Estimates (29), (31) and (32) contain the volume fractions of the BLs. The characteristic velocity U is for example a root mean square (rms) velocity probing the large-scale turbulence (and thus the wind) in the system. Furthermore, the derivation of the last two relations makes use of Pohlhausen's idea of the passive advection of the temperature by the Blasius flow [31]. In case of $Pr \gg 1$ one has to take the full Blasius profile into account. In case of $Pr < 1$, *i.e.*, when the viscous BL is well nested in the thermal BL, temperature advection can be approximated by the constant outer velocity.

In an extension of the theory [32] a full functional dependence for the relations $Nu(Ra, Pr)$ and $Re(Ra, Pr)$ was suggested that incorporates the varying ratio of both BL thicknesses with respect to each other when the Prandtl number is changed, *i.e.*, with (11) and (27) one obtains $\delta_v/\delta_T = Nu/(2\sqrt{Re})$. Interpolations of the form $f(x) = (1 + x^4)^{-1/4}$ are used to model the crossover between the four main different regimes. A second aspect has to be incorporated, as the Prandtl number grows, the Reynolds number of the wind will decrease which would cause δ_v to diverge theoretically. Physically this is prohibited by the fact that the viscous BL cannot grow beyond H. This introduces an *a priori* unknown cut-off Reynolds number Re_c. This transition to the saturation of the growth of δ_v is again modeled by a function $g(x) = (1 + x^4)^{-1/4}$. This results in the following set of equations:

$$(Nu-1)RaPr^{-2} = c_1\frac{Re^2}{g(\sqrt{Re_c/Re})} + c_2Re^3, \tag{33}$$

$$Nu - 1 = c_3\sqrt{RePrf\left[\frac{2aNu}{\sqrt{Re_c}}g\left(\sqrt{\frac{Re_c}{Re}}\right)\right]} + c_4RePrf\left[\frac{2aNu}{\sqrt{Re_c}}g\left(\sqrt{\frac{Re_c}{Re}}\right)\right]. \tag{34}$$

Equation (33) follows from (16) and (25), eq. (34) from (17) and (26). The coefficients c_1 to c_4 and the cut-off Reynolds number Re_c follow when experimental data are matched by a nonlinear fit. An additional sixth fit parameter is the prefactor a from (27). The resulting Reynolds number dependence was further discussed in [33].

Another modification of the scaling theory was proposed later in [34]: decomposition (26) was replaced by

$$\langle\epsilon_T\rangle_{V,t} = \langle\epsilon_T\rangle_{pl,t} + \langle\epsilon_T\rangle_{bg,t}, \tag{35}$$

which splits the thermal dissipation rate into contributions coming from the plumes (pl) and the turbulent background (bg). Again both terms contain the corresponding volume fractions. It was expected that the plume contributions arise mostly from the side walls while the background part is dominantly in the center of the cell. On this basis, predictions for the local convective heat flux J_c and the temperature fluctuations T_{rms} were developed and found to be in agreement with laboratory experiments [35,36] and recent direct numerical simulations [37].

3.5 Scaling in the ultimate regime of convection

3.5.1 Kraichnan's classical scaling theory

Which global heat and momentum transport do we get if we increase the Rayleigh number to very large values? On the basis of classical mixing length arguments [31] which were adapted by a turbulent boundary layer structure, Kraichnan derived the following transport laws [38] for the regime of convection now known as the *ultimate regime*:

$$\left.\begin{aligned} Nu &\sim \left[\frac{RaPr}{(\overline{\kappa}^{-1}Pe_T\ln Ra)^3}\right]^{1/2} \\ Re &\sim \left[\frac{RaPr^{-1}}{4\overline{\kappa}^{-1}Pe_T\ln Ra}\right]^{1/2} \end{aligned}\right\} \; Pr \leq 0.15 \tag{36}$$

and

$$\left.\begin{aligned} Nu &\sim \left[\frac{RaPr^{-1/2}}{(\overline{\kappa}^{-1}(Pe_TRe_s)^{1/2}\ln Ra)^3}\right]^{1/2} \\ Re &\sim \left[\frac{RaPr^{-3/2}}{4\overline{\kappa}^{-1}(Pe_TRe_s)^{1/2}\ln Ra}\right]^{1/2} \end{aligned}\right\} \; 0.15 < Pr \leq 1, \tag{37}$$

where $Re_s = u_\tau \delta_{\rm vis}/\nu$ is the constant shear Reynolds number with $\delta_{\rm vis}$ being the thickness of the viscous sub-layer. $Pe_T = u_z(\delta_T)\delta_T/\kappa$ denotes the Péclet number at which the thermal BL becomes turbulent. This constant is not known and has to be estimated. The Reynolds number was here defined as $Re = U(H/2)H/(2\nu)$ where U is the *rms* velocity in the bulk.

We will discuss in brief the derivation of the (36) as an example. In this case $\delta_v < \delta_T$, such that outside the thick thermal boundary layer, turbulent eddy viscosity and diffusivity determine the dynamics. For distances $\delta_T \leq z \leq H/2$ we can thus assume that $|(\mathbf{u}\cdot\nabla)u_z| \sim g\alpha\theta$ from (7) and $|(\mathbf{u}\cdot\nabla)\theta| \sim u_z {\rm d}\langle T(z)\rangle/{\rm d}z$ from (9) hold. When power laws for velocity, temperature fluctuation and mean temperature are assumed, this results in

$$u_{z,rms} \sim z^{1/3}, \quad \theta_{rms} \sim z^{-1/3}, \quad \langle T(z)\rangle \sim z^{-1/3}, \quad (38)$$

a scaling that was already suggested by Priestley [39] and which results in a transport law for the heat of $Nu \sim Ra^{1/3}$. The shortcoming of this derivation is that it completely ignores the shear effects which arise when the velocity boundary layer becomes turbulent in case of very large Rayleigh numbers. Kraichnan recognized that once the Reynolds number is sufficiently high a logarithmic profile for velocity fluctuations is established. Considering low Prandtl numbers where the viscous boundary layer is completely nested in the thermal boundary layer, $\delta_v < \delta_T$, the turbulence develops outside the sublayer and supports the heat transfer. The intensity of the velocity fluctuations at the edge of the thermal boundary layer is now estimated by u_τ and thus the Péclet number is now taken as

$$Pe_T = \frac{u_z(\delta_T)\delta_T}{\kappa} \to \frac{u_\tau \delta_T}{\kappa}, \quad (39)$$

which is an important point. In the center the heat transport is assumed to be dominated by the convective current and is approximately given by

$$J_c \sim \frac{1}{2} u_{z,rms}\theta_{rms} \approx \frac{1}{2} U\theta_{rms}, \quad (40)$$

with both *rms* values taken at $z \approx H/2$. Energetically, a balance between kinetic and potential energy holds in the bulk

$$\frac{1}{2}u_{z,rms}^2 \approx \frac{1}{2}U^2 \approx \frac{H}{2} g\alpha\theta_{rms}. \quad (41)$$

Deriving θ_{rms} from (41), inserting it in (40) and recalling the definition of Nu, leads to an expression for turbulent convective flows (see also the exact relation (16))

$$NuRa = Pr^2 Re^3. \quad (42)$$

The logarithmic law of the wall (18) can be rewritten to

$$\frac{U(H/2)}{u_\tau} + \frac{1}{\overline{\kappa}} \ln\left(\frac{U(H/2)}{u_\tau}\right) \approx \frac{1}{\overline{\kappa}} \ln Re + B, \quad (43)$$

and gives as first approximation $u_\tau \simeq U(\frac{1}{\overline{\kappa}} \ln Re)^{-1}$. Recalling now eq. (11) that states $\delta_T = H/(2Nu)$ and using eq. (39) one finds

$$Nu = \frac{u_\tau H}{2\kappa Pe_T} \simeq \frac{UH}{2\kappa Pe_T \frac{1}{\overline{\kappa}} \ln Re} \simeq \frac{RePr}{2Pe_T \frac{1}{\overline{\kappa}} \ln Re}, \quad (44)$$

which results together with (42) in relation (36) for Nu. The expression for Re follows the same way. In this last step, $2\ln Re \approx \ln Ra$ has been applied to get (36).

Kraichnan derived the ranges for the Prandtl numbers in (36) and (37) from the ranges that should hold for the thickness scales in his boundary layer models. Interestingly, $Nu \sim Ra^{1/2}$ is a scaling that is derived as a rigorous upper bound to the turbulent heat transport when applying variational calculus to the Boussinseq equations (7) to (9). More details can be found in [40–42] and are also discussed in [14,16].

3.5.2 Grossmann-Lohse theory for turbulent BL

In case of $Pr \leq 1$, the scaling laws $Nu \sim (RaPr)^{1/2}$ and $Re \sim (Ra/Pr)^{1/2}$ without logarithmic corrections follow also from the model [15] when (16) and (17) and the bulk contributions (28) and (30) are taken. In case of $Pr \gg 1$ it was shown in [15] that $Nu \sim Ra^{1/3}$ is obtained. Logarithmic corrections cannot appear in this derivation since they are based on the assumption of a laminar viscous BL.

Only recently, the ansatz (25) was adapted to a turbulent BL [43] by splitting energy dissipation into contributions of the viscous buffer (*vsl*) and the logarithmic layer (*ll*)

$$\langle\epsilon\rangle_{V,t} = \langle\epsilon\rangle_{vsl,t} + \langle\epsilon\rangle_{ll,t}, \quad (45)$$

together with the assumption that the logarithmic layers from the top and bottom fill the whole cell. Again both averages contain the corresponding volume fractions. Repeating estimates similar to (28) and (29) one gets now

$$\langle\epsilon\rangle_{ll,t} \sim \frac{\nu^3}{H^4} Re^3 \left(\frac{u_\tau}{U}\right)^3 \left[\frac{1}{\overline{\kappa}} \ln\left(Re\frac{u_\tau}{U}\right) + B\right], \quad (46)$$

$$\langle\epsilon\rangle_{vsl,t} \sim \nu \frac{u_\tau^2}{z_\tau^2}\frac{z_\tau}{H} \sim \frac{\nu^3}{H^4} Re^3 \left(\frac{u_\tau}{U}\right)^3, \quad (47)$$

where (46) is obtained by averaging the well-known relation $\langle\epsilon(z)\rangle = u_\tau^3/(\overline{\kappa}z)$ along the logarithmic layer up to $z = H/2$. The energy dissipation resulting from the sustained logarithmic layer will dominate and together with (16) one gets

$$NuRaPr^{-2} \sim Re^3 \left(\frac{u_\tau}{U}\right)^3 \left[\frac{1}{\overline{\kappa}} \ln\left(Re\frac{u_\tau}{U}\right) + B\right]. \quad (48)$$

The second relation for the thermal dissipation rate has to be worked out. One can expect that the thermal boundary layer is turbulent too. If we assume that the von Kármán constants in the logarithmic laws for flow and temperature are about the same one can use (cf. (10))

$$Nu \approx \frac{-(\overline{\kappa}u_\tau z - \kappa)\frac{\partial\langle T(z)\rangle_{A,t}}{\partial z}}{\kappa\Delta T/H}, \quad (49)$$

and thus

$$Nu \sim RePr \left(\frac{u_\tau}{U}\right)^3 \left[\frac{1}{\overline{\kappa}} \ln\left(Re\frac{u_\tau}{U}\right) + B\right]. \quad (50)$$

The global transport laws for heat and momentum follow thus for non-asymptotic Pr to

$$Nu \sim Ra^{1/2}Pr^{1/2} \left(\frac{u_\tau}{U}\right)^3 \left[\frac{1}{\overline{\kappa}} \ln\left(Re\frac{u_\tau}{U}\right) + B\right], \quad (51)$$

$$Re \sim Ra^{1/2}Pr^{-1/2}. \quad (52)$$

The effective scaling exponent of turbulent heat transfer which follows for the ultimate regime can be estimated to $0.35 \lesssim \beta_{\text{eff}} \lesssim 0.42$.

4 Experimental and numerical methods

After the discussion of the scaling theories for the global transport laws we turn now to a discussion of the results of measurements and direct numerical simulations. Before starting, we review in short some methods and parameter ranges.

4.1 Working fluids and accessible parameter ranges

As shown in table 1, convection flows in Nature and technology appear frequently at very high Rayleigh number. Recalling the definition of Rayleigh number in (1), the parameters one can change are α, ΔT, H, ν, and κ. Systematic changes of H are not easy to realize and often lead to changes in the aspect ratio Γ introducing thus an additional variation. Moreover, the range of validity of the Oberbeck-Boussinesq approximation is usually estimated by [21]

$$\alpha\Delta T < 0.1\text{–}0.2, \quad (53)$$

thus limiting the variations of this parameter. Many experiments at moderate and high Rayleigh numbers have been performed in water because these experiments allow several possibilities of visualization [44–46]. The highest Rayleigh numbers reached for convection in water are those of the group in Hong Kong [46] which reached $Ra = 5 \times 10^{12}$ at $Pr = 4$ and those of the group in Lyon [47,48] in which $Ra = 4 \times 10^{12}$ at $Pr = 2$ was obtained. The majority of the laboratory experiments are conducted in cylindrical cells; some studies have been performed in rectangular convection cells [49–54].

Low-Prandtl number convection requires working fluids such as mercury (Hg). Tsuji *et al.* [55] performed such experiments in the range $10^6 \le Ra \le 7 \times 10^{10}$ with Prandtl number $Pr = 0.024$. Velocities in mercury have been measured with ultrasonic techniques.

Convection for Prandtl numbers around unity (in particular $Pr = 0.7$) can be established in several working fluids. One way to change the Rayleigh number without changing the cell size is to use gases near the critical point (see also sect. 7.1). In this case the physical parameters of the fluid such as kinematic viscosity, thermal diffusivity and thermal expansion coefficient can be varied by changing the distance to the critical point.

Several gases have been used at ambient temperatures: argon Ar [56,57], nitrogen N_2 [56–58], helium He [56,59], ethane C_2H_6 [60], sulfur hexafluoride SF_6 [56,58,61,62], and air [63]. Globally, the range $60 < Ra < 10^{15}$ of Rayleigh numbers has been spanned with gases.

When helium is cooled down to a few kelvins (the critical point is at 5.19 K for a pressure of 2.27 bar) the advantages of this working fluid become manifold: first of all low-temperature experiments benefit from a very good thermal isolation because of the cryogenic vacuum. Second, very poor thermal capacity of the metal together with a very large thermal diffusivity allow a short response to temperature variations at the plates. The first experiment with low-temperature helium was done by Threlfall [64] in 1975 which covered a range of Rayleigh between $60 \le Ra \le 10^9$. Afterwards numerous other experiments were performed for an increasingly large range of Rayleigh numbers revealing a complex behavior and probably a strong dependence on the boundary conditions which will be discussed in detail below. The highest accessed Rayleigh number of $Ra = 10^{17}$ is still the one in the laboratory experiment by Niemela *et al.* [65].

An extreme case in terms of system size is occupied by the actually largest thermal convection laboratory experiment in the world, known as the "Barrel of Ilmenau (BOI)" with a height and diameter of up to seven meters [63]. The working fluid is air at ambient temperature and pressure. Convection in the BOI can span a range of $10^6 \le Ra \le 2 \times 10^{12}$ and aspect ratio $100 \ge \Gamma \ge 1$. While global quantities such as Nu are not easy to measure, one has full access to the boundary layers close to the top and bottom plates which will be discussed in detail in sect. 5.3.

4.2 Direct numerical simulations

Direct numerical simulations discretize the equations of motion on a spatio-temporal grid and resolve all features of the turbulent flow down to the smallest physical scale which is on average the Kolmogorov length η_K for $Pr \le 1$ or the Batchelor scale $\eta_B = \eta_K/\sqrt{Pr}$ for convection at $Pr > 1$. Nearly all present three-dimensional DNS of the Boussinesq equations (7)–(9) at higher Rayleigh and finite Prandtl numbers are based on one of the following numerical techniques:

- Second-order finite-difference scheme on a staggered non-equidistant computational grid for cylindrical cell [66,67].
- Fourth-order finite-volume method on non-equidistant computational grid using the Chorin ansatz for sustaining incompressibility for cylindrical and rectangular cells [68].
- Spectral element method using Legendre polynomials for arbitrary geometries [69–71].
- Pseudospectral method with periodic side boundaries, such as in [72,73].

Beside this list of 3D DNS, simulations in a two-dimensional setting using fourth-order finite-difference methods [74,75] should be mentioned.

A resolution criterium for the mean grid spacing $\tilde{\Delta}$ in DNS has been discussed first by Grötzbach [76]. His criterion is a translation of the resolution requirement in pseudospectral simulations of box turbulence, which is given by $k_{max}\eta_K = \sqrt{2}N\eta_K/3 \geq 1$ (with $N = 2\pi/\tilde{\Delta}$), to the present case. It states that[1]

$$\tilde{\Delta} \leq \begin{cases} \pi\eta_K = \pi(\nu^3/\langle\epsilon\rangle)^{1/4}, & Pr \leq 1, \\ \pi\eta_B = \pi(\nu\kappa^2/\langle\epsilon\rangle)^{1/4}, & Pr \gg 1. \end{cases} \quad (54)$$

Recent DNS showed that this criterion is not sufficient in particular for the thin boundary layers close to the plates. In refs. [27,77,78] new criteria have been suggested which incorporate the strong vertical variation of gradients and thus of the kinetic energy dissipation rate. Based on Blasius theory the following estimates for $10^6 \leq Ra \leq 10^{10}$ were suggested for the number of grid points N_{BL} inside the thermal and viscous boundary layer [78] ($Pr = 0.7$):

$$N_{BL}^T \geq 0.35 \times Ra^{0.15}, \qquad N_{BL}^v \geq 0.31 \times Ra^{0.15}. \quad (55)$$

If the boundary layers become turbulent this criterium might not be sufficient anymore. It is immediately clear that these constraints on the resolution slow down the progress towards higher Rayleigh numbers which can be made in DNS. Currently, DNS for cylindrical cells with $\Gamma = 1/2$ can reach $Ra = 2\times10^{12}$ [79]. Since the numerical effort grows with Γ^2 when larger aspect ratio cells are considered, recent DNS at $\Gamma = 1$ achieved $Ra = 3 \times 10^{10}$ only, but requiring almost the same number of grid points [80] as the former case for $\Gamma = 1/2$.

5 Experiments and simulations for Ra $\lesssim 10^{12}$

5.1 Nu-Ra scaling

In fig. 2 we summarize the results of the dependence $Nu(Ra)$ for several recent experiments in cylindrical cells. Data are given in a compensated plot $NuRa^{-1/3}$ *versus* Ra. For an ensemble of older data, we also refer here to the reviews [14,16]. The first impression is that the data which we summarized in this figure scatter. Several points should be mentioned:

- Data points have been obtained for different experimental conditions. Different materials for the plates and the side walls were used.
- The experiments were conducted at partly different aspect ratios varying between 0.23 and 20.

[1] Grötzbach used in his original work [76] the so-called Corrsin scale $\eta_C = \nu^{3/4}/\langle\epsilon\rangle^{1/4}$ in case of $Pr \geq 1$. It has to be replaced by the Batchelor scale η_B since an increasing fraction of temperature filaments is advected in the viscous-convective range when Pr increases.

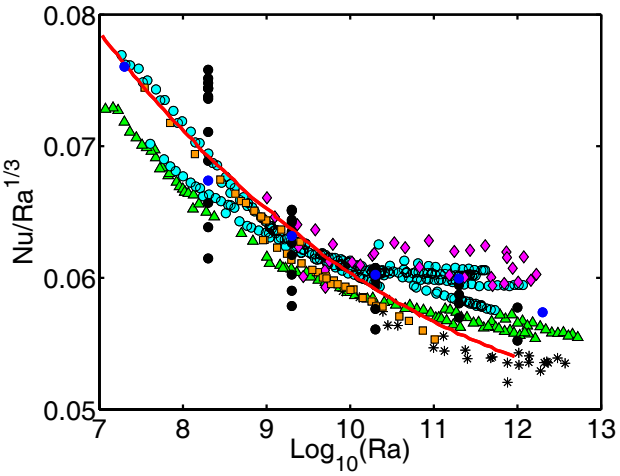

Fig. 2. Heat transport as a function of the Rayleigh number. Data are shown in compensated power law plot for several experiments: cyan circles for [44,45] ($0.23 \leq \Gamma \leq 6$, $Pr = 4.38$), green triangles for [46] ($0.67 \leq \Gamma \leq 20$, $Pr \approx 4$). Both series involve finite conductivity corrections of plates and side walls. Furthermore, black asterisks are for [48] and orange squares for [59]. These data contain finite conductivity corrections of the side walls. Magenta diamonds are for [57], black circles for DNS [79] ($\Gamma = 0.23$, $0.5 \leq Pr \leq 10$), and the blue circles for [79] ($\Gamma = 1/2$, $Pr = 0.7$). The red solid line represents the curve as obtained from the Grossmann-Lohse theory based on (33) and (34).

- Different systems of thermal insulation and different feedback controls of heating and cooling at the top and bottom plates have been used.
- The presence of side walls is a non-negligible problem for all experiments at smaller aspect ratios. They will always have a small, but non-zero conductivity and heat capacity. The first-order effect of the thermal conductivity has been calculated and modeled in refs. [81, 82] and also discussed in DNS by Verzicco [83]. Those corrections are differently calculated, but lead to very close values for the side-wall corrections of up to three percent. The corrections are based on the fact that a part of the heat flux is injected into the flow through the lateral walls. All the data measured contain one of the two proposed side-wall corrections depending on the authors.

It is yet an open point if further effects exist that may influence the flow and thus the heat transfer measurements. For example, thermal plumes might get locked in some special configuration due to slight temperature inhomogeneities at the plates which might affect the overall thermal dissipation. Such effects might become increasingly important in the very high-Rayleigh-number regime, as we will discuss later.

Another important issue is the behavior of the large-scale circulation (LSC) that is always established in a closed convection cell, at least for the values of Rayleigh numbers discussed here. When convection sets in, plumes of the same type (cold or hot) have the tendency to cluster

giving rise to a large-scale flow [84]. It has been found in experiments [85] and DNS [27] that the morphology of the large-scale circulation depends on the form of the cell and the aspect ratio, particularly at intermediate Rayleigh numbers. For example in a cell with aspect ratio of one essentially one LSC roll is expected. If the container is perfectly cylindrical and no symmetry-breaking mechanism exists this roll shows a slow precession which has been discussed in [16]. If the cell has an aspect ratio larger or smaller than one, two or more circulation rolls can be present next or on top of each other, respectively. The large-scale circulation can switch between these states (see *e.g.* [67,85–87] or the review [16]). The importance of the recirculation zones at the edges of the cell is another point that might become important in particular for smaller aspect ratios.

The answer to the question of whether the LSC influences the Nusselt number seems to be yes, but the influence is decreasing with increasing Rayleigh number. While DNS at $Ra = 10^7$ observe variations of up to 10% when the LSC structure changes, very recent measurements of Weiss and Ahlers [86] found a variation of about 1.6% in the Nusselt number between one-roll and two-roll state for $Ra = 10^{12}$.

Small changes of order of 2% have been also found when tilting the cell in [47,85]. These are evidently consequences of the action of gravity on the large scale flow. While the authors in ref. [47] suggest that gravity can fix a one-roll state, Xi and Xia [85] suggest that once the flow is locked the frequency of plumes is reduced. In [88] a bimodality of the Nusselt number of about 7% was found for $10^8 \le Ra \le 10^{11}$, $0.73 \le Pr \le 10$ and $\Gamma = 1/2$. Roche *et al.* [88] also suggest that this difference is linked to the coexistence of one-roll and two-rolls states. The difference is here larger than in [86] which itself was larger than the one measured in [85]. We also remark, as noted in [86], that not in all the experiments the two-roll flow has been found. It is therefore possible that external conditions as walls or thermal symmetry breaking can lock the structure of the flow. Xia suggested [89] furthermore that the influence of the Prandtl number has to be taken into account. As a final remark, we can stress that the effect is small for sufficiently high Rayleigh numbers. The smallness of the effect is not really surprising; it is in good agreement with several other measurements [50,90–92] in which the large scale flow has been disturbed or clearly suppressed and in which the Nusselt number has been found to vary by at most 5%.

Summarizing the figure, we can nevertheless state that the different data sets agree rather well, keeping in mind that we have a compensated plot. The largest difference is about 20%. Given the measurement comparisons in many other turbulent flows this underlines a significant progress which has been obtained in the past decade on the experimental side. The data underline clearly that the 1/3 power law is not really satisfactory for the Rayleigh number range. The figure also reports the expression of the Grossmann-Lohse theory [15] (see (33) and (34)) with the coefficients calculated for $\Gamma = 1$ and a fit of the data of [93] and [94], as reported in [16]. We conclude that the fit works quite well taking into account the diversity of experimental data which are reported here. The advantage of the scaling theory is that it can combine crossovers between different parameter regimes and scalings which would not be possible with simple power laws. None of the states in the present range of Rayleigh numbers reflects a "pure" power law scaling. Coefficients c_1 to c_4 calculated from other data at larger aspect ratios would be certainly interesting.

5.2 Local near-wall structures and global circulation

5.2.1 Thermal plumes and streamwise streaks

As in all other wall-bounded turbulent flows, characteristic near-wall structures are observed in turbulent convection. The most important ones are the *thermal plumes*, fragments of the thermal boundary layer which detach permanently from the cold and the hot plate and move into the bulk of the cell which is accompanied by a broadening of these structures due to diffusion and mixing by turbulent fluid. Plumes are the coherent structures that carry a large fraction of the heat into the convection layer. Their extension into the bulk depends on Pr and Ra. Higher Pr favor plumes with narrow stems which can reach far into the bulk due to the small diffusivity. Hot and cold plumes do not collide, but groups of hot (or cold) plumes merge and give life to the large scale flow, the LSC. A fraction of the plumes (filaments) can thus travel from one plate to the other along the lateral side walls and transport heat. Among the first who investigated their typical vertical structure in experiments are Spangenberg and Rowland [95] and later Sparrow, Husar and Goldstein [96]. Figure 3 shows a plume visualization made for convection in air at $Ra = 1.3 \times 10^{10}$ in the boundary layer of the Barrel of Ilmenau.

Although the thermal plumes can be experimentally visualized today in several ways, quantitative criteria to extract plumes are yet an open problem. Several criteria have been suggested which are based on thresholds of certain quantities. These could be the temperature [97], the vertical velocity [98] or the skewness of the temperature derivative [99]. Plume extraction is also possible by local measurement of the thermal dissipation rate [100]. Numerical experiments by Shishkina and Wagner [101,102] compared several criteria based on the thermal dissipation rate ϵ_T or the local heat current $J_T = J_c + J_d$ (see eq. (10)). The following criteria have been suggested:

- Threshold on the temperature T. This would extract the red colored hot filaments in fig. 4 (top)
- Threshold on the product of thermal dissipation rate and temperature [101], $\epsilon_T T$.
- Local maxima of a conditional mean thermal dissipation [102], which is given by

$$\Lambda = \frac{\langle \epsilon_T \mathcal{H}(T_k, T_{k+1}) \rangle_{A,t}}{\langle \mathcal{H}(T_k, T_{k+1}) \rangle_{A,t}}, \qquad (56)$$

with a temperature window composed by two Heaviside functions $\mathcal{H}(T_k, T_{k+1}) = \mathcal{H}(T - T_k) - \mathcal{H}(T - T_{k+1})$.

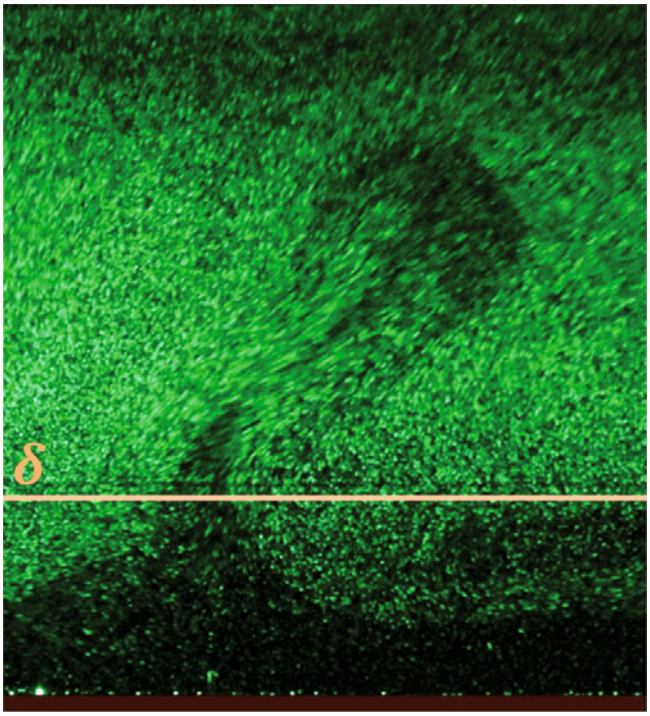

Fig. 3. Vertical snapshot of a thermal plume that detaches from the boundary layer in the Barrel of Ilmenau. The red bottom area is the heating plate. The viscous boundary layer thickness δ_v is indicated by the horizontal line and the symbol "δ". The Rayleigh number is $Ra = 1.3 \times 10^{10}$ and the Prandtl number is $Pr = 0.7$. Visualization has been made with DEHS particles, the same which are used for particle image velocimetry. (Figure from Ronald du Puits, TU Ilmenau, Germany.)

– Positive values of convective heat flux, based on the temperature fluctuations [52,26], $u_z\theta > 0$.

All these criteria allow to decompose the turbulent volume into a plume-dominated fraction V_{pl} and a rest, the turbulent background V_{bg}, which we mentioned already at the end of sect. 3.4 (see also [34]). The numerical simulations show that with increasing Rayleigh number the plume volume fraction decreases while the background increases [101].

On the basis of such a decomposition several geometric analyses were performed [102] such as the length of the plumes, the thickness or their diameter. Parallel to this effort, the morphological evolution of thermal plumes has been studied in detail using the thermochromic-liquid-crystal technique for convection in water up to $Ra = 8 \times 10^{10}$ [103,104]. A second series of experimental studies was focussed on the plume structure for different Prandtl numbers of $Pr = 0.7$, 5.2 and 602 and for Rayleigh numbers between $10^5 \leq Ra \leq 10^{11}$ [54,105].

The main findings from the structural analysis can be summarized as follows: The skeleton of plumes is mostly composed of sheet-like plumes (see also fig. 4 (top)). At the connection points of this skeleton the sheet-like plumes get convoluted. Here, they can evolve into mushroom-type plumes which are associated with a strong vertical vorticity component $\omega_z = \partial_x u_y - \partial_y u_x$ and a strong local upward flow into the bulk as found for $Pr = 5.4$ in [102] and $Pr = 0.7$ in [106]. The detachment of the thermal plumes is accompanied by a three-dimensional velocity dynamics [80]. With increasing Rayleigh number, experiments and DNS demonstrate that the area occupied by individual plumes decreases while their number increases which is in line with a growing fragmentation of the thermal plumes and increasing instability of the boundary layer. In [104] it

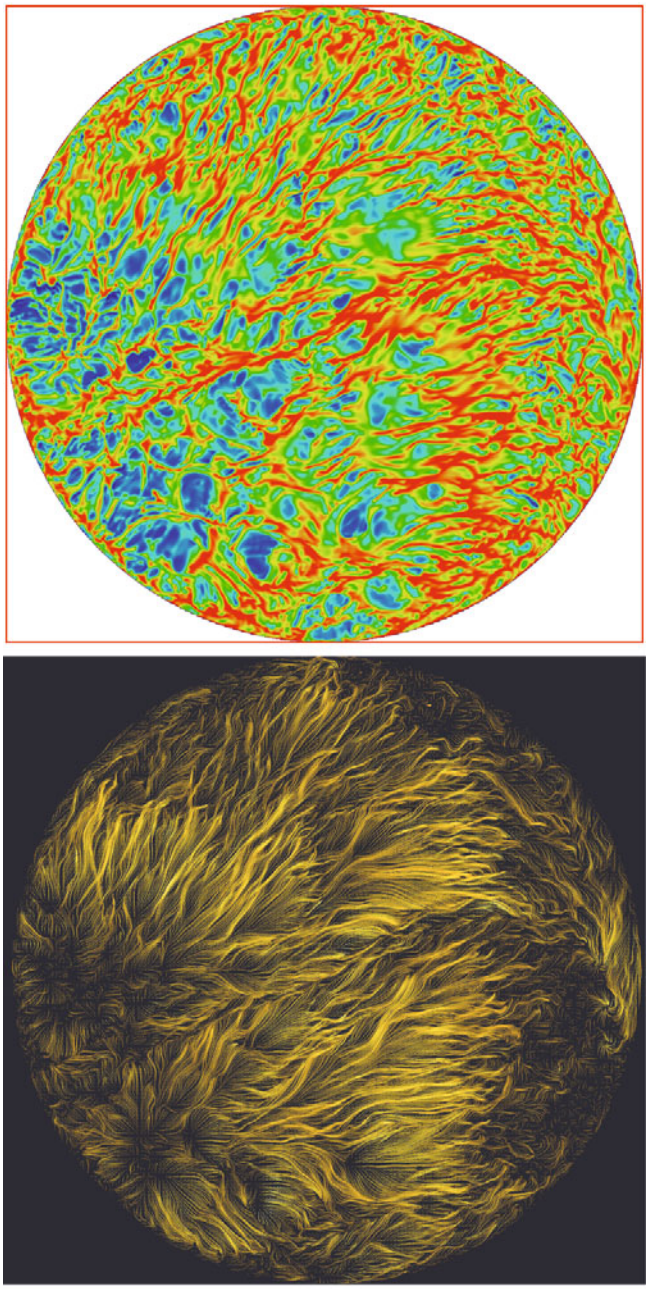

Fig. 4. Horizontal cut at the thermal boundary layer thickness at $z = \delta_T$. DNS are at $Ra = 3 \times 10^{10}$, $Pr = 0.7$ and $\Gamma = 1$ [80]. Data are exactly the same as in fig. 5. The top figure shows the temperature field T, the bottom figure the streamlines in a view from the top. The mean direction of the flow is from the lower left to the top right in the bottom panel.

is found that geometric measures such as length $\mathcal{L}$, width $\mathcal{W}$, area $\mathcal{A} = \mathcal{L}\mathcal{W}$ and perimeter $\mathcal{P} = 2(\mathcal{L} + \mathcal{W})$ are log-normally distributed. For $Pr \simeq 5$ Zhou and Xia [104] report the relations

$$N_s \simeq 1.4\, Ra^{0.29\pm0.03}, \qquad N_m \simeq 0.41\, Ra^{0.32\pm0.03}, \quad (57)$$

where N_s and N_m are the numbers of sheet-like and mushroom-like plumes, respectively. Puthenveettil *et al.* [54] found in their measurements that

$$N_s \sim Ra^{1/3}, \quad (58)$$

in combination with a weak Prandtl number dependence. Indeed, one can see that both experiments end with scaling exponents close to the direct Nusselt number determination with respect to the Rayleigh number. However, the number of plumes cannot give directly the correct scaling $Nu(Ra)$. The determination of the heat flux and thus the Nusselt number would require a weighting by their volume fraction and their intensity, $u_z\theta$.

Much less effort has been spent on the analysis of coherent structures of the velocity field close to the walls since they are less easily accessible. Furthermore, a large-scale circulation which varies spatially and in magnitude complicates such an analysis significantly. Zocchi *et al.* [107] reported wavy structures in the boundary layer from their water experiments. Later Haramina and Tilgner [108] reported streaky flow structures as they would be generated by pairs of streamwise counter-rotating vortices in a non-normal amplification mechanism. They visualized these structures by dye for convection in a rectangular water tank where the large-scale circulation was probably locked. They also showed that similar mechanisms are at work as they are well-known from plane shear flows and isothermal boundary layers [109]. Such studies will to our view become more relevant as one has to understand the transitional behavior of the boundary layer for increasing Rayleigh number much better. Figure 5 displays streamwise flow structures which have been aligned with the instantaneous direction of the LSC. The red isocontours indicate that the flow is mostly accelerated in comparison to the mean. This might be related to the active role of the temperature which comes here into play.

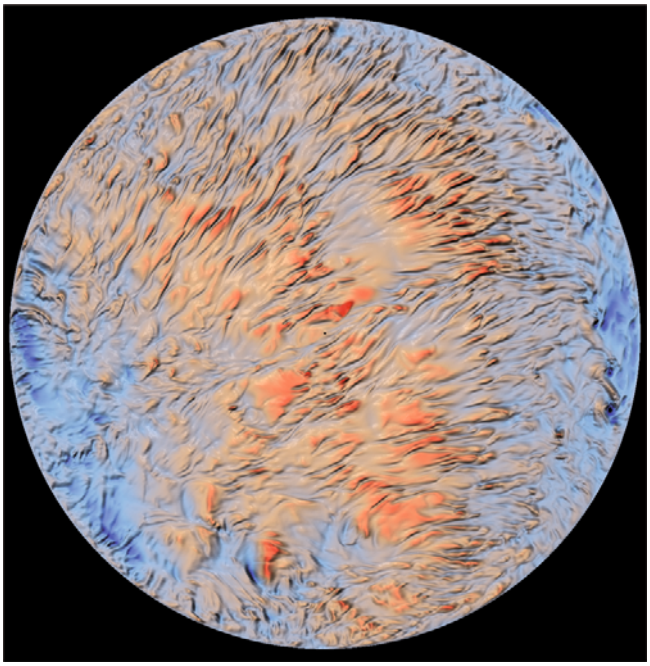

Fig. 5. Visualization of streamwise flow structures inside the boundary layer. The horizontal cut is done at the thermal boundary layer. Contours of the horizontal velocity fluctuations along the instantaneous LSC direction are shown. Red for $u_\parallel = +028U_f$ and blue for $u_\parallel = -0.34U_f$. Data are exactly the same as in fig. 4.

5.2.2 Spatial structure of large-scale circulation

We started to discuss the role of the large-scale circulation (LSC) on the global transport already in sect. 5.1. In the last years, both experiments and DNS, have investigated its spatial structure in a detailed way (see also [16] and references therein for further studies). Particle image velocimetry measurements in cylindrical convection cells revealed how the thermal plumes synchronize their emission and how they organize to a LSC [110]. The coherent large-scale organization of the flow was detected by velocity time series taken instantaneously at different side wall locations at $z = H/2$. The large-scale circulation evolves together with smaller recirculation zones close to the side walls. They have been visualized in detail in cells with $\Gamma = 1/2$ in DNS by Verzicco and Camussi [67] for $Pr = 0.7$ and in experiments by Sun *et al.* [111] for $Pr = 5.3$. The latter measurements detected also a stochastic azimuthal motion of the LSC. This permanent change of the mean direction of the LSC is accompanied by a irregular temporal variation of its mean velocity magnitude. This is also the outcome of very recent high-resolution DNS by Wagner *et al.* [112] and Shi *et al.* [80] in which access to the full three-dimensional velocity field is given. These oscillations have been also measured earlier in the BOI [113].

In order to determine a mean orientation over a limited time interval, Brown and Ahlers [116] suggested an indirect way via the temperature measurement at several points at the side wall. Temperature is then fitted by a function $T(\mathbf{x}_m) = A\cos((2\pi m/N_\phi) + \phi_{\rm LSC})$ where N_ϕ is the number of azimuthal nodes possible with the finite number of probes and $m = 1 \ldots N_\phi$. The phase shift $\phi_{\rm LSC}$ characterizes the mean orientation of the LSC over a finite time interval. As stated above, all DNS [77,112,80] showed that this orientation can fluctuate strongly. Wagner *et al.* [112] provided therefore a comparison of five different functions to determine finite-time interval average of $\phi_{\rm LSC}$ which were for example based on the local heat flux $J_c + J_d$ or the azimuthal vorticity component and found that the heat flux criterion works best. Moreover the LSC is found to evolve on different time scales. There is a fast mode that is associated with the looping inside the cell. This motion can be interrupted by cessations and flow reversals as studied by statistical models *e.g.* in

refs. [114–117]. Petschel *et al.* [118] and Mishra *et al.* [119] studied such reversals on the basis of primary flow modes as obtained from their DNS data sets. Furthermore, the mean directions of flow at the top and bottom are not the same, suggesting a circulation roll with a combination of torsion and an off-centre sloshing (see *e.g.* [85]). On top of these fast variations a quasi-adiabatic slow mode exists which is characterized by a slow change of the orientation angle of the LSC. This variation can be obtained by averaging over several loop times and was observed in [80].

The LSC is always a full three-dimensional flow obeying a significant cross-flow component (see the flow snapshot in the bottom panel of fig. 4) as long as it is not constrained to a slim rectangular cell as in the experiments by Xia and co-workers (see *e.g.* [53]).

All the studies show that the LSC provides already a richness of flow features which will certainly affect the dynamics in the boundary layers. Simulations allow also to quantify the amount of heat that is carried with the LSC. Bailon-Cuba *et al.* [27] and van der Poel *et al.* [87] showed in simulations that the change in the LSC configuration causes jumps in the Nusselt number, in particular for the smaller aspect ratios, *i.e.*, the range where the majority of the laboratory experiments are conducted. In [27], a systematic variation of the scaling exponents in the Nu-Ra scaling was detected. The studies suggest also that the jumps in the Nusselt number become smaller for increasing Ra (see also our discussion above in 5.1). Experiments and DNS indicate that the circulation velocity of the LSC decreases with increasing Rayleigh which can be attributed to an increasing fragmentation of the plumes, the main driver of the LSC. Additional systematic studies are however necessary to characterize the phenomenon. Furthermore, a convection flow at larger Pr helps to diminish the jumps in Nu [87].

5.3 Boundary layer dynamics

Although the importance of the boundary layer is recognized already for a long time, its detailed vertical structure is not easily accessible with a sufficiently high resolution for $Ra > 10^8$, both, in experiments and DNS. Among the first experiments on the thermal boundary layer structure we mention Chillà *et al.* [49] and Belmonte *et al.* [56]. Velocity boundary layers over a certain range of Rayleigh numbers have been measured first by Xin *et al.* [120] and Adrian [121]. Measurements of boundary layer profiles beyond $Ra \sim 10^{10}$ require large experimental devices such as the BOI for the convection in air [63] or high-resolution particle image velocimetry for convection in water [53].

Recently, these boundary layer studies focused on comparisons of the measured mean profiles of velocity and temperature with those from Prandtl-Blasius-Pohlhausen theory [31] of forced convection (since there is a prescribed outer flow) and those from natural convection [122,123]. The classical boundary layer theories rely in both cases on a two-dimensional and steady flow. In the Prandtl-Blasius-Pohlhausen model the temperature is additionally assumed to be passively advected and pressure gradients are zero. The active nature of the temperature field is incorporated in the natural convection case and fluid motion is initiated by pressure differences. Within the natural convection BL framework models for the individual plume dynamics have been suggested, *e.g.* [124]. However, a shear flow across the plates is absent in those plume models. Perturbative expansions from both limiting cases to the so-called mixed convection have been done in [125, 126]. These extensions remain two-dimensional models.

Mean velocity profiles in the boundary layer yield deviations from the predicted laminar Blasius profiles [127–129] when they are analyzed in the classical way. Du Puits *et al.* [127] concluded from their work that the deviations from the Blasius shape arise due to the thermal plumes which permanently detach from the thermal boundary layer. Direct numerical simulations (DNS) by van Reeuwijk *et al.* [130] for Rayleigh numbers up to 10^8 support deviations from a Blasius boundary layer. They compared the vertically integrated horizontal pressure gradient with the shear stress at the edge of the BL. This pressure term is not zero as in the Blasius case.

However, different analyses and experimental conditions can improve the agreement with the Prandtl-Blasius-Pohlhausen theory

- A dynamical rescaling with an instantaneously defined boundary layer thickness incorporates the temporal fluctuations of the boundary layer [129,131,80]. The instantaneous thicknesses $\delta_v(t)$ and $\delta_T(t)$ are defined as the intersection points between the linear slope to the profile taken at the wall and the tangent at first maximum of the profile.
- Quasi-two-dimensional cells [129] and two-dimensional DNS [128,131] constrain the large-scale circulation (see also 5.2.2) to a plane and suppress their full three-dimensional dynamics, in particular the oscillations of the orientation. This will also result in a better agreement with the classical boundary layer theory.
- The higher the Prandtl number of the working fluid the better the thermal boundary layer is nested in the velocity boundary layer and the less the permanent detachment of thermal plumes disrupts the velocity boundary layer dynamics at fixed Rayleigh [129].

The scaling of both thicknesses with respect to the Rayleigh number comes however close to the predictions from the classical boundary layer theories. Such comparison requires the additional determination of the relation $Re(Ra, Pr, \Gamma)$ in order to relate the obtained scaling with the theories for forced and natural convection. Wagner *et al.* [112] report scalings of $\delta_T \sim Ra^{-0.285\pm0.003}$ and $\delta_v \sim Ra^{-0.238\pm0.009}$ for $Pr = 0.7$, $\Gamma = 1$ and Rayleigh numbers up to 10^9. Lam *et al.* [132] verified a dependence $\delta_v/H \simeq 0.65 Ra^{-0.16} Pr^{0.24}$ for a cylindrical cell $\Gamma = 1$, with $6 \leq Pr \leq 1027$ and $10^8 \leq Ra \leq 10^{10}$. More recent experiments in a narrow rectangular cell by Sun *et al.* [53] revealed $\delta_v/H \simeq 4.95 Ra^{-0.27\pm0.01}$ and $\delta_T/H \simeq 6.10 Ra^{-0.32\pm0.05}$ for $Pr = 4.3$ and $10^9 \leq Ra \leq 10^{10}$. We can see that different cell geometries and different Prandtl numbers can affect the scaling. This is a further support for the fact that the LSC structure, which itself is sen-

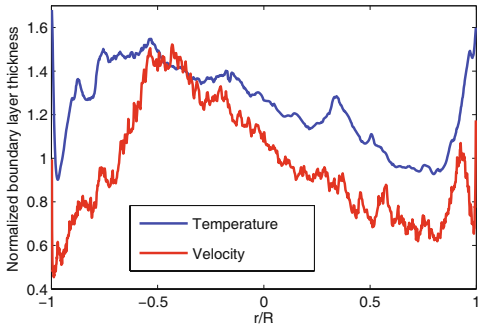

Fig. 6. Normalized boundary layer thicknesses of temperature, $\delta_T(r)$, and velocity, $\delta_v(r)$, across the whole convection cell. Data are from a DNS by Wagner *et al.* [112] for $Ra = 10^9$, $\Gamma = 1$, and $Pr = 0.786$. They are normalized by $\delta_T = H/(2Nu)$ and the most probable velocity BL thickness, respectively. They are obtained by time averaging for each r in the plane aligned with the LSC.

sitive to geometry and aspect ratio, is important for the dynamics in the BLs.

Recent high-resolution DNS of the boundary layer dynamics [80,112] brought further insights on the 3D structure close to the walls. As already said above, both works showed that the LSC is a three-dimensional flow in the cylindrical cell. The horizontal components of the pressure gradient are strongly fluctuating in the whole convection cell. The probability density functions of $\partial p/\partial r$ and $r^{-1}\partial p/\partial \phi$ yield fatter tails when determined in the boundary layers in comparison to the bulk [80]. The boundary layer thicknesses taken in a plane which is aligned with the LSC grows in the mean downstream direction as shown for the data taken from [112] in fig. 6. Such significant variations of the thickness of both boundary layers have also been detected in water experiments [133,134]. This implies that all velocity BL measurements depend very sensitively on the position at which they are taken. There is also no indication that the profiles grow with $\delta_v \sim r^{1/2}$ as in the Blasius case. To summarize, the numerical studies up to $Ra \sim 10^{10}$ show three-dimensional and time-dependent boundary layers with a local dynamics that can be divided into short sequences of a plume detachment and a re-laminarized post-detachment dynamics [80].

On top of these aspects which we have discussed so far, one has to keep in mind that the transitional character of the boundary layers increases as the Rayleigh number grows. Recent DNS demonstrated actually that the dynamical rescaling of the thermal boundary layer works increasingly insufficient when Ra grows which indicates that the temporal fluctuations in the boundary layer become increasingly important [135]. For Rayleigh numbers beyond 10^{12}, logarithmic temperature profiles have been detected close to the side-walls very recently which seem to indicate that the turbulent regime of the BLs is reached [136].

5.4 Role of roughness

The importance of the boundary layer dynamics for the Nusselt number is also clearly shown by experiments in which roughness has been introduced at the plates. Roughness effects are indeed important for all practical situations, either for industrial applications or for convection in Nature: an atmospheric boundary layer is rarely found over smooth surfaces. Several experiments with different kinds of roughness have been realized in the past years. All results agree on one point: the presence of roughness increases the Nusselt number drastically compared to the smooth-plate situation. The way how the Nusselt number increases seems to depend on the particular kind of roughness and the range of accessible Rayleigh numbers. We report the works done in the recent years and we refer to [137] for further past studies. All the experiments presented here were conducted in cylindrical cells.

In the work of Du and Tong [137] roughness is established by pyramids of height h_0 in cells of $\Gamma = 1$ and 1/2. Roughness was varied within $0.08 \leq h_0/H \leq 0.45$ for $10^8 < Ra < 10^{10}$. The Nusselt number increased by 76%, but the exponent of the scaling law $Nu \simeq Ra^{0.29}$ was unchanged with respect to the case of smooth plates. It should be noted here that an increase by 76% is much larger than what can be expected from the increased surface at the plates. Roche *et al.* [138] used triangular-shaped grooves for both plates and the walls. When the thermal boundary layer thickness δ_T is of the same order of magnitude as the roughness height, a transition of the heat transport law towards $Nu \simeq Ra^{1/2}$ develops. They attributed this finding to a triggered transition to turbulence in the boundary layers —the Kraichnan regime [38]. Later Qiu *et al.* [139] applied the same kind of roughness as Du and coworkers (now machined directly into the plates). They found an increase of the Nusselt number by 60%, but now with a scaling of $Nu \simeq Ra^{0.37}$, *i.e.*, different from the smooth case. The authors attributed the differences to the thermal properties of the plates as linked to different material (copper in [139] instead of brass in [137]) and the differences in the fabrication of the rough plates.

The most recent experiments have been realized in Lyon for $10^9 < Ra < 10^{12}$ for $\Gamma = 0.5$ and 2.5. In this case, the cell had asymmetric plates. The top plate was smooth while the bottom plate was rough. The roughness is obtained by small cubes with $h_0/H = 0.01$ or 0.2. Such experiment allows to test the influence of roughness and the independence of both boundary layers at the plates simultaneously. Thanks to the measurement of the bulk temperature it is possible to define independently the two boundary layers. The convection at the smooth plate was found to be in very good agreement with previous measurements in the same cell with two smooth plates (see fig. 2). A 1/3 scaling law for $Nu(Ra)$ is found, at least for the highest Rayleigh numbers. For the rough plate the situation is completely different and shows that the two plates can be considered as being independent. When the thermal boundary layer thickness δ_T is of the same order as the roughness height h_0, the heat flux begins to increase as $Nu \propto Ra^{1/2}$. The global heat flux becomes larger at higher Rayleigh numbers because of the increased exchange surface. It seems also to be clear from those results that the Nusselt number is completely determined by the local behaviour of the boundary layer.

The reasons for this transition to enhanced heat transort are still not clear. Two processes can be involved: a transition to turbulence of the boundary layer as proposed by [138] or an increase of plume production due the interaction between the inner flow and circulations at roughness elements. By repeating the experiment in a cell of $H = 20$ cm and a Reynolds number being ten times smaller, the authors find the same transition, again for $h_0 \simeq \delta_T$. This result seems to favor the second hypothesis. When δ_T became sufficiently small the typical law of a smooth plate has to be found. In ref. [137] h_0 is always greater than δ_T which rationalizes the unchanged scaling exponent of the rough plate case. As an open point remain the differences with [139] which operates in the same range as [137].

Finally, we mention DNS by Shiskina and Wagner [140] for a two-dimensional cell for $Ra \leq 10^8$. They show that an increase of the surface which is linked to an increasing roughness cannot explain the augmented value of the Nusselt number. Up to $Ra = 10^8$, the Nusselt number is increased, but the scaling law $Nu(Ra)$ remains unchanged. The parameter h_0 is the length which characterizes the roughness and h_0/H seems to be a supplementary nondimensional parameter that characterizes the problem. The lateral distance between the small obstacles could also play a significant role as suggested in [140]. The influence of this spacing has never been tested experimentally in RB cells.

5.5 Bulk flow without boundary layers

One point, which was also investigated in the last years, is the possibility to separate the dynamics of the boundary layer and the bulk in experiments. For bulk-dominated convective turbulence, power laws (see sects. 3.5.1 and 3.5.2) have been suggested which have a simple physical interpretation: the heat and momentum transport is a purely inertial process. To verify this hypothesis, it is necessary to have a bulk flow independent from the thermal boundary layer. In this case, a sustained temperature gradient which is necessary to drive convection, cannot be concentrated in the boundary layers. It has to be a mean gradient over the whole flow. The dimensionless parameters have consequently a slightly different definition compared to (1):

$$Ra = \frac{g\alpha\,\overline{\partial T/\partial z}\,L^4}{\nu\kappa}\,, \tag{59}$$

and

$$Nu = \frac{\langle u_z T\rangle_{A,t}}{\kappa\,\overline{\partial T/\partial z}} = \frac{Q}{\kappa\,\overline{\partial T/\partial z}}\,, \qquad Re = \frac{UL}{\nu}\,, \tag{60}$$

where Q is the injected power and L is a typical length that depends on the flow.

One possibility is to use DNS [141] in which a flow in a box with periodic boundary conditions is sustained in convective motion by the application of a constant mean gradient. Caution is then necessary for the amplification of the motion with respect to the vertical direction [142]. In these simulations the heat transport is completely inertial and $Nu \simeq (RaPr)^{1/2}$ has been found. From the experimental point of view boundaries cannot be completely avoided because a container for the fluid is necessary. Two experiments have approached this ideal situation: a salt driven channel flow developed in Bangalore and a thermal convective channel developed in Lyon. The first experiment was realized by Cholemari *et al.* [143,144] in a vertical pipe connecting two chambers in which a difference of salt concentration is imposed at the beginning of the experiment. The Schmidt number is $Sc = 670$, such that the situation is equivalent to a high-Pr flow, the aspect ratio is $\Gamma = 1/9$ and the tube has a circular cross section. In this case the equivalent of Nusselt number cannot be directly measured. It is inferred from the measurement of the concentration fluctuations using the equivalent of eq. (16). The flow is completely mixed by colliding plumes resulting in large horizontal velocity fluctuations. The mean velocity is found to be equal to zero. The experiments obtained $258 < Re < 545$ and $7.5 \times 10^7 < Ra < 3.34 \times 10^8$. The equivalent of a Rayleigh number can be calculated by taking $(1/\rho)\partial\rho/\partial z$ instead of $\alpha\partial T/\partial z$. Scale L is now the pipe diameter. Again, $Nu \sim Ra^{1/2}$ and $Re \sim Ra^{1/2}$ as predicted for a bulk flow.

The second experiment by Gibert *et al.* [145–147] is inspired by [148] and conducted in a channel connecting two chambers, a hot at the bottom and a cold at the top. In this way, the channel is fed continuously with hot and cold fluid and maintained in a stationary convection state. The working fluid is water with a Prandtl number varying between $4 < Pr < 6$. Two successive channels have been used in this experiment. They have a square cross-section and $\Gamma = 1/2$ and $1/4$. The Nusselt number is determined from the injected power into the flow and the direct measurement of the temperature gradient inside the channel as given in (60). The experiment showed a particular large-scale flow organization. Hot and cold fluid streams in form of columns along one side of the channel in each case and changes sides spontaneously. Therefore an intrinsic length $L_n = \langle\theta^2\rangle^{1/2}/\overline{\partial_z T}$ is defined. This length is equal to horizontal size of the channel for $Re < 600$ and grows as $\log Re$ afterwards. All the parameters in (59) and (60) are now based on this length and $10^5 < Ra < 4 \times 10^7$ and $150 < Re < 3500$. By conditioning the analysis to one counter stream flow configuration, it was found that Reynolds stress and mean shear stress differ from zero. Evidently an unconditioned average gives zero Reynolds stress and zero shear. The detected transport laws are again

$$Nu \sim Ra^{1/2}Pr^{1/2}, \qquad Re \sim Ra^{1/2}Pr^{-1/2}, \tag{61}$$

in agreement with the results from scaling theories. An open point is the behaviour of the new length scale L_n and its dependence on the Reynolds number. Schmidt *et al.* [149] simulated recently a circular pipe (as in [143]), but with a thermal transport as in [145] applying periodic boundary condition at the top and bottom. The DNS show

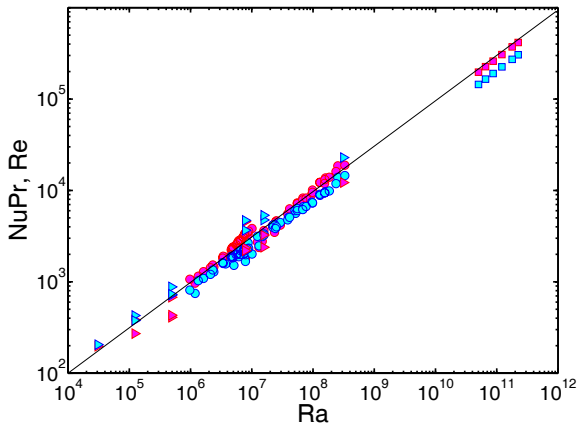

Fig. 7. Reynolds number (cyan symbols), and the product $NuPr$ (magenta symbols) as a function of the Rayleigh number for several channels setups. Triangles denote DNS data of [149] for $0.125 < \Gamma < 0.5$. Circles denote data of [147] and squares stand for data of [144]. The solid line indicates the generic power law $Ra^{1/2}$. The length scale in [147] has been normalized in order to have the same definition as in [144] for small Reynolds number.

the existence of a non-stationary dynamics at low Rayleigh number and larger aspect ratio. Complete mixing is obtained when the aspect ratio is decreased as in [144]. They also found a scaling (61) showing that the lateral boundary layers at the side walls do not affect the heat transfer. All data which are reported in fig. 7 are in very good agreement, showing that the absence of top and bottom boundaries leads to a more "universal" situation for the scaling laws. This kind of flow seems to be an interesting example for studies of turbulent thermal convection without boundary layers and could have implications for processes in the ocean or the atmosphere.

5.6 Lagrangian studies of thermal convection

The Lagrangian perspective in which statistical properties of turbulence are sampled along the trajectories of fluid particles provided qualitatively new insights into the relation between flow structures and extreme statistical events, in particular for the case of homogeneous isotropic turbulence (see [150] for a comprehensive review). In thermal convection, Lagrangian studies allow to study the local mechanisms of the turbulent transport which are connected with the strongly varying thermal plumes. Such studies require to measure temperature and velocity at once and were pioneered with small neutrally buoyant temperature sensors which were optically tracked in a water convection cell at $Ra = 3 \times 10^{10}$ and measured the temperature [52,151] (see fig. 8). Thus positive correlations between the vertical velocity and temperature fluctuations, $u_z\theta > 0$, could be monitored while the probe circulates with the mean wind through the cell. As we discussed in sect. 5.2.1 this is one way to detect plumes.

Only recently, a second series of Lagrangian convection experiments using particle tracking velocimetry was conducted in a water cell for $6 \times 10^8 \leq Ra \leq 10^{11}$ [152]. Ni *et al.* [152] showed that turbulence conditions in the center of the convection cell are comparable to homogeneous isotropic turbulence by probing the Heisenberg-Yaglom relation for the acceleration variance [153,154]. This relation is given by

$$\langle a_z^2 \rangle = a_0 \frac{\langle \epsilon \rangle^{3/2}}{\nu^{1/2}} = a_0 \frac{\kappa^4}{H^6} Pr(Ra\, Nu)^{3/2}, \qquad (62)$$

where (16) has been used. Their prefactor a_0 when plotted as a function of the Taylor microscale Reynolds number R_λ was consistent with numerical and other laboratory experiments. Here, R_λ was obtained by a measurement of the kinetic energy dissipation and the velocity fluctuation directly in the cell center.

The inhomogeneity of turbulent convection is manifest when lateral and vertical tracer pair dispersion are compared as in DNS with periodic side boundaries for $\Gamma = 2, 4$ [73,106]. Since the vertical dispersion is limited by the height of the cell, horizontal dispersion takes over when the diffusive regime is approached for very large times. The latter resembles qualitatively the properties which are known from three-dimensional box turbulence [155] supposed that the convection cell has a sufficiently large aspect ratio [156]. Both, experiments [152] and DNS [73] demonstrated that the horizontal accelerations yield PDFs, $p(a_x/a_{x,rms})$ and $p(a_y/a_{y,rms})$, that have fatter tails than the PDF of the vertical acceleration component, $p(a_z/a_{z,rms})$. The latter component, a_z, is connected with the plume detachment which can thus be considered as a gradual process which has been discussed already above.

The experimental and numerical studies [52,156] in cylindrical convection cells showed that the Lagrangian convective heat current $J_c(\mathbf{x}, t) = u_z T(\mathbf{x}(t; \mathbf{x_0}, t_0), t)$ and thus the normalized upward Lagrangian local heat transport

$$Nu_L = 1 + \frac{H}{\kappa \Delta T} u_z \theta(\mathbf{x}(t; \mathbf{x_0}, t_0), t), \qquad (63)$$

fluctuates strongly and can even obtain negative values as shown in fig. 8(c) where $Nu_L(t)$ is plotted. The corresponding PDF is strongly skewed to the positive amplitudes. The resulting mean over the whole particle ensemble and time, $\langle Nu_L(t) \rangle_{L,t}$, corresponds with the Nusselt Nu which is usually determined from the Eulerian fields [156].

6 Experiments and simulations for Ra $\gtrsim 10^{12}$

As table 1 indicates, most geo- and astrophysical convection processes are associated with Rayleigh numbers beyond 10^{12}. The hope of the physicists is to find an asymptotic regime of high-Rayleigh-number convection in the Boussinesq approximation (see sect. 3) which can be related to at least some of those applications of thermal convection in Nature. As pointed out in the last sections already, this ultimate regime of convection is connected

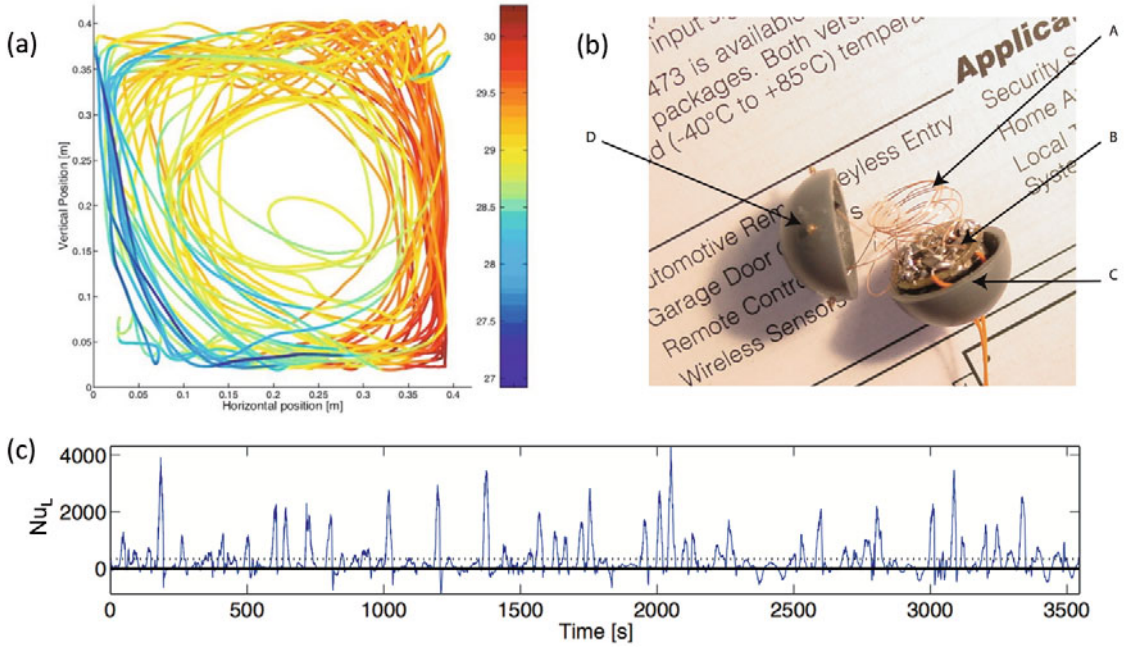

Fig. 8. Lagrangian studies of turbulent Rayleigh-Bénard convection in a cell of the form of a parallelepiped with dimensions $40 \times 40 \times 10\,\mathrm{cm}$ at a Rayleigh number $Ra = 3 \times 10^{10}$ [52]. (a) Trajectory of probe in the cell colored by the temperature which varies between 27 °C and 31 °C (see color bar). (b) Photography of the Lagrangian temperature probe before closing the capsule with a diameter of 21 mm. It shows the antenna (A), the radio frequency emitter (B), the battery (C), and the on-off switch (D). (c) Time series of $Nu_L(t)$ as defined in eq. (63) taken from the experiment [52].

Table 2. List of experiments at very high Rayleigh numbers in alphabetic order with respect to location. The highest Rayleigh numbers have been obtained usually for the smallest aspect ratios. All cells are cylindrical. All the helium experiments are at low temperature. The last experiment was designed to study non-Boussinesq convection as discussed in sect. 7.1.

Location	Ra	Fluid	Γ	Ref.
Brno	10^7–10^{14}	He	1	[170]
Chicago	10^6–10^{15}	He	1/2,1, 6.7	[157,158]
Eugene	10^7–10^{17}	He	1/2	[65]
Trieste	10^7–10^{14}	He	1, 4	[163]
Göttingen	10^{12}–10^{15}	SF_6	1	[58,62]
Grenoble	10^3–10^{14}	He	0.23, 1/2, 1	[92,160]
Rehovot	10^8–10^{15}	SF_6	1/2, 1	[61]

to a transition to turbulent boundary layers for the flow and the temperature [38]. While DNS just start to enter the range of $Ra \sim 10^{12}$ [79], several experiments have been conducted at such high Rayleigh numbers as listed in table 2.

From experimental point of view, the results reveal a complicated picture and indicate that a unique universal regime is not easy to reach as shown in fig. 9. We summarize all the high-Rayleigh-number experiments in low-temperature helium together with the measurements in compressed SF_6 and the DNS of [79].

A first inspection confirms what was said previously: a good agreement for Rayleigh number less than 10^{12} (about 20% of difference between the data) is observable. Larger differences up to about 100% arise for larger Rayleigh numbers which might be triggered by different flow states. To understand the complexity behind both panels better, we discuss the measurements in their "historical" appearance. All data are obtained again in cylindrical cells. In 1989, measurements started in Chicago for a very large range of Rayleigh numbers, first for $\Gamma = 1$ [157] and $10^6 < Ra < 10^{11}$ followed by $\Gamma = 0.5, 6.7$ [158] and $10^6 < Ra < 10^{14}$. Scaling laws $Nu \propto Ra^\beta$ with $\beta \simeq 0.287$ only slightly dependent on Γ were obtained. The corresponding data shown in the graph are for $\Gamma = 1/2$ where the material parameters of helium have been recalculated as in [92].

Measurements in Grenoble followed for $\Gamma = 1/2$ and $10^3 < Ra < 10^{14}$ [159,160]. The experiments used a special home-made thermocouple detector in order to measure the difference of temperature between the plates directly with a precision of $10\,\mu$K. It also allowed to cover a very large range of Rayleigh numbers with the same density. The measurements agreed with the ones in Chicago up to $Ra = 7 \times 10^{11}$; afterwards a transition to a state of enhanced heat transport was detected which followed a scaling of $Nu \sim Ra^{0.38}$. This power law is compatible with Kraichnans asymptotic law including logarithmic corrections as in eq. (37) and the Grossmann-Lohse prediction (51). Interestingly, the measurements in Chicago showed a similar multi-stability at about the same Rayleigh number. There it was observed that they

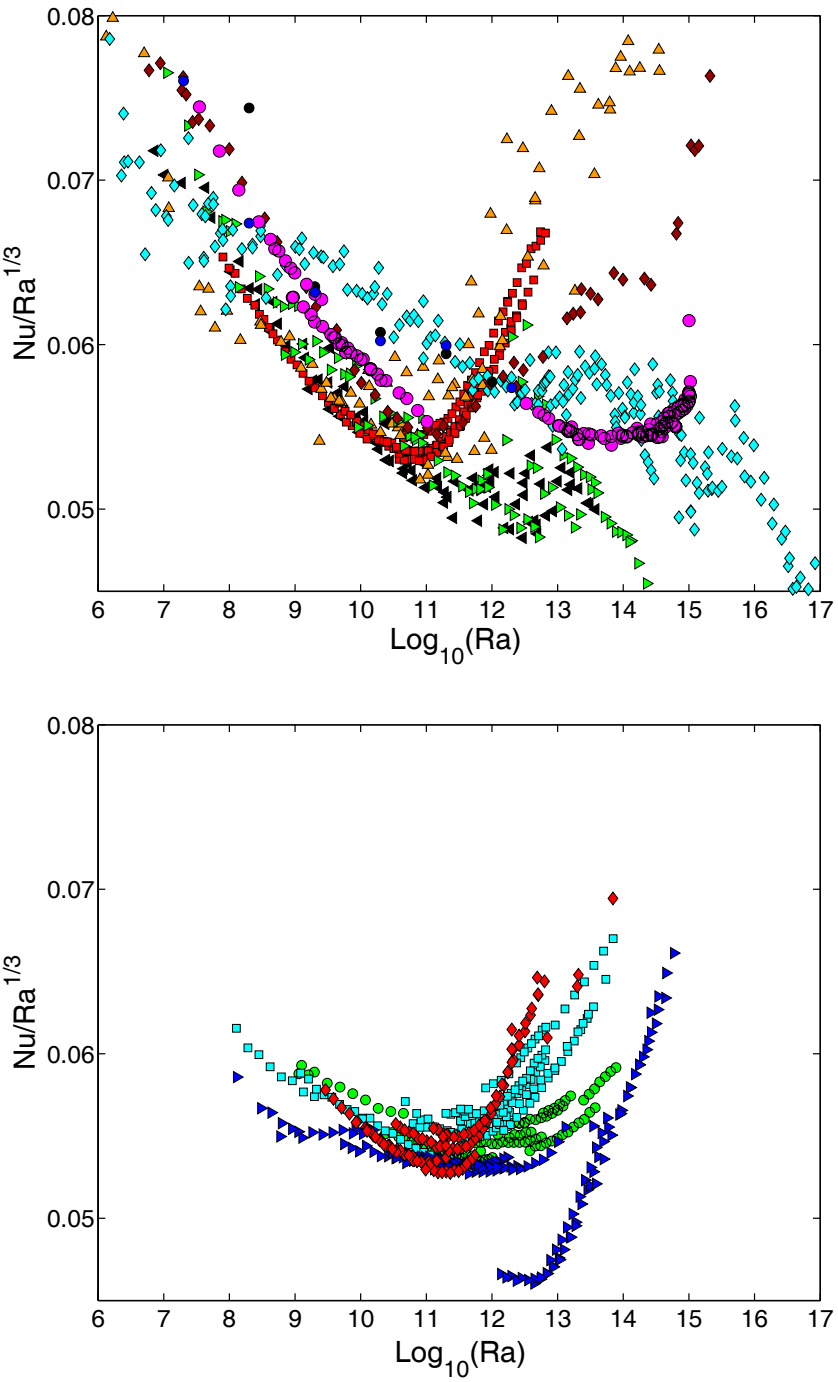

Fig. 9. Top: heat transport as a function of the Rayleigh number in a compensated power law plot. Experiments and DNS at very high Ra are collected: green triangles pointing to the right for Chicago at $\Gamma = 1/2$ [157,158] with wall corrections [92]; orange triangles pointing upward for Grenoble [160] corrected for the finite conductivity of the walls. Red squares are for Grenoble experiments [92] at $\Gamma = 1$. Black triangles pointing to the left are for Brno [170] corrected for the wall conductivity. Magenta circles stand for Göttingen [62,58]. Blue circles are for DNS [79] at $Pr = 0.7$ and $\Gamma = 1/2$; black circles for $Pr = 2$ and $\Gamma = 0.23$. Cyan diamonds stand for Eugene (Oregon) [65] with wall corrections and brown diamonds for Trieste at $\Gamma = 1$ (wall correction included). See also table 2. Bottom: heat transport as a function of the Rayleigh number in a compensated power law plot. The experiments with different limit conditions were all realized in Grenoble. Red diamonds are for new measurements in the same cell as Chavanne *et al.* [160], here given for comparison. Green circles are for side walls covered with paper, cyan squares for a flange cell, and blue triangles pointing to the right for a cell with $\Gamma = 0.23$ [92].

go erratically toward an enhanced transport state. However, for $Ra \gtrsim 10^{13}$ data from the experiment in Chicago followed a branch below an effective scaling exponent of $\beta = 0.38$.

Further cryogenic helium experiments followed in Eugene (Oregon) [65] in a cell of $H = 1\,\mathrm{m}$ for $10^7 < Ra < 10^{17}$ with a power law $Nu \sim Ra^{0.31}$ covering a range of ten orders of magnitude of the Rayleigh number. Those data were successively recalculated in order to take the effect of wall conductivity into account [161] which resulted in a new scaling exponent of $\beta = 0.323$ in agreement with [57] (data in fig. 2). The experiment was reassembled in Trieste for $\Gamma = 1$ and $\Gamma = 4$ [162,163]. The data of $\Gamma = 1$ showed a transition to enhanced transport for $Ra > 10^{12}$. For $\Gamma = 4$, such transition can also be observed, but in a range outside the validity of the OB approximation (cf. eq. (53)). We wish to note that a transition to turbulence in the BL is not necessarily affected by non-Boussinesq effects, both effects can co-exist. New measurements for $\Gamma = 1$ and 4 found a hysteresis in the $Nu(Ra)$ graph [164] in combination with a saturation towards a 1/3-scaling at high Rayleigh numbers. This hysteresis was attributed to a non-Boussinesq effect not documented before. An alternative interpretation is here possible: a transition to turbulent BLs is followed by a non-Boussinesq effect which suppresses a crossover to an enhanced heat transport at very high Rayleigh numbers. Hystereses of global quantities in closed flows have been recently reported in a counter-rotating turbulent von Kármán flow [165] and in Rayleigh-Bénard experiments with asymmetric plates: a smooth plate on the top and a rough one at the bottom [48]. The authors of [164] give arguments against this interpretation. The large-scale Reynolds number is too small at their value of Ra to cause a transition to turbulence in the boundary layers. We will get back to this point later.

Roche *et al.* conducted recently a series of experiments in helium to test the sensitivity of heat transport with respect to boundary conditions. They used convection cells with brass plates in order to investigate the influence of the thermal conduction of the plates [166], with thick lateral walls, with external heating which destroys the small recirculation patterns in the corner of the cell, with obstacles to test the impact of the large scale flow, and with paper along the side wall [92]. All the modifications affected the Rayleigh number at which the system crosses over into the ultimate transport regime. They had a small impact on the scaling exponent β. Only two remarkable changes were obtained. In the cell with paper along the lateral walls, in which an enhanced heat capacity can be inferred, the transition is shifted towards $Ra \sim 10^{13}$ and the scaling exponent is smaller. The threshold depends additionally on the aspect ratio which took values of $\Gamma = 0.23, 1/2$ and 1 in the series. Very roughly the transition Rayleigh numbers varies as $Ra \sim \Gamma^{-2.5}$, *i.e.*, the smaller Γ the higher the threshold for the same Prandtl number, here $Pr \simeq 1$. Those last findings underline to our view the subtle influence of the lateral walls. Gautier and Roche [167] studied also the fluctuations in the boundary layer indirectly via measuring local fluctuations at the plate for low temperatures. When compared with temperature fluctuations in the bulk, they found that both follow the same power law as a function of Ra up to the transition threshold. Afterwards, the temperature fluctuations in the boundary layer increased significantly.

Measurements in the "Uboot" of Göttingen [62] with SF_6 were conducted in a cell of $\Gamma = 1/2$ and $H = 2.2\,\mathrm{m}$. They show a good agreement with the recalculated measurements of [161] up to $Ra = 10^{13}$ followed by a transition towards the ultimate regime and a scaling of $Nu \sim Ra^{0.38}$ as in the Grenoble measurements and compatible with Kraichnan law including the logarithmic corrections [38] (sect. 3.5.1) and the Grossmann-Lohse model for the turbulent BL [43] (sect. 3.5.2). However the prefactor of the power law differed strongly between both experiments. Two further findings of the experiment should be mentioned. The transition threshold changes slightly when the external temperature changes. Furthermore, they obtain a state of very low conductivity when the cell is not completely sealed with respect to the outer reservoir (open sample) [58]. Both findings show clearly that the transition is very sensitive to external conditions for the very high Rayleigh numbers.

One line of argumentation for a transition to the ultimate regime at $Ra \gg 10^{12}$ is based on the fact that a shear Reynolds number has to be exceeded for which a transition to a turbulent boundary layer can be triggered or for which a turbulent boundary layer is sustained [162, 62,164]. Such a shear Reynolds number can be defined in several ways, either as $Re_s = u_\tau \delta_v/\nu$ [38] or as

$$Re_s^* = \frac{U\delta_v}{\nu} \tag{64}$$

in ref. [15]. Definition (64) is relevant here. However it leaves several possibilities for the definition:

- Quantity U can be a root-mean-square velocity in the bulk or for the whole cell or the mean wind velocity at the edge of the boundary layer.
- Thickness δ_v can be interpreted as δ_{99}, the thickness of the BL at which the streamwise velocity recovers 99% of the original inflow velocity, as the displacement thickness δ_1 or as the momentum displacement thickness δ_2. For the classical Blasius theory, these three thicknesses differ already by a factor of more than 7 [31] and they are not measurable in all existing very-high-Rayleigh-number experiments.

On top of this, the transition Reynolds number can take different values. Preston concluded from his measurements that sustained turbulence over a flat plate requires $Re_s^* = U\delta_2/\nu > 320$ [168]. In [169] a threshold $Re_s^* = U\delta_1/\nu = 420$, in [31] $Re_s^* = U\delta_1/\nu = 520$ is referenced. These numbers are still above shear Reynolds numbers that would correspond to $Ra \sim 10^{11}$. However they have been obtained for a canonical flat plate boundary layer flow, while the BL in turbulent convection will be permanently disrupted by thermal plumes as we discussed in sect. 5.3. This might trigger a transition to turbulence at lower Reynolds numbers. Moreover it is also possible

that the ultimate regime corresponds to a situation in which a coherent LSC becomes very weak, which would be consistent with the finding of [86] that the large scale flow seems to lose is strength with increasing Rayleigh number.

The behavior with respect to the Prandtl number for $Ra < 10^{12}$ have been discussed in several works as summarized in [16]. The results are in good agreement with the Grossmann-Lohse model [15]. At very high Rayleigh numbers the Prandtl number dependence seems to be more subtle. First we state that predictions (36) and (37) from Kraichnan [38] and (51) and (52) from Grossmann and Lohse [43] report different scaling laws with respect to finite Pr. In recent experiments in Grenoble, Pr was systematically varied in different cells [92]. The transition to enhanced transport appears for $Pr \sim 1$ with a very weak Prandtl number dependence. Measurements in Trieste show the transition for $Pr \simeq 1$, but at a higher Rayleigh number. The measurements in Göttingen observe the transition at higher Ra with a nearly constant $Pr \simeq 0.7$. From this perspective the measurements are not in contradiction to each other. If the LSC triggers the transition to the ultimate regime small Pr could be favorable, if it is linked to velocity fluctuations inside the BL the Prandtl number could have a more complicated influence.

Most recently a further helium experiment in Brno [170] was conducted. In this cell of $\Gamma = 1$ no transition towards an ultimate regime has been found. The scaling continues as $Nu \sim Ra^{1/3}$ up to $Ra = 4.6 \times 10^{13}$. Those points are realized in the same range of Pr as the measurements in Trieste and at the same distance from the critical point as stressed by the authors which challenges the non-Boussinesq arguments in [162,163].

In the graph of fig. 9(a) DNS of Stevens *et al.* [79] for $\Gamma = 1/2$ are also reported. They show no evidence of a transition to the ultimate regime at $Ra \sim 10^{12}$. In ref. [77] the authors show that sufficiently high grid resolutions are necessary near all walls in order to determine the Nusselt number correctly (see also the discussion in sect. 4.2). In turn one could thus conclude from these DNS that imperfect adiabatic side walls might have an influence on the transition. Further DNS for $\Gamma = 0.23$ and several Prandtl numbers have been also conducted [79]. The Nusselt number is in very good agreement with the corresponding measurements in Grenoble for $Pr = 0.7$, but gives a higher value at $Pr = 2$. To summarize here, we see that the present experiments give no unique picture at the very high Rayleigh numbers and show a high sensitivity with respect to boundary conditions.

7 Beyond the classical Rayleigh-Bénard case

As we already stated in the introduction (see table 1), many convective flows in Nature and technology go beyond the simplest case, the OB regime of Rayleigh-Bénard convection. In the last part of this review, we therefore discuss two extensions in more detail which have obtained growing interest in the last years. In sect. 7.1, we present recent attempts to investigate deviations from the OB model [23,24] which has been presented in sect. 2. In sect. 7.2, phase changes are incorporated into the OB model which lead to statistical properties that differ also from those of the OB case.

7.1 Non-Oberbeck-Boussinesq effects

Two pathways lead to non-Oberbeck-Boussinesq (NOB) effects in turbulent convection. In gases, this path is related to deviations from the incompressibility limit. The anelastic approximation (5) is a first weak compressibility effect which is for example incorporated in atmospheric convection that exceeds layers of height $H \approx 2$ km. Stronger compressibility effects and thus large variations of the fluid properties can arise when the working fluids are operated in the vicinity of their critical points as done in helium [171], in ethane [172], or in SF_6 [61].

The latter experiment by Burnishev and Steinberg [61] is of particular interest since it reports the absence of a property that is usually assigned with NOB convection —the breaking of the up-down-symmetry. While in [171, 172] the deviation of the centre temperature from the algebraic mean, $T_{\rm ref} = (T_{\rm bottom} + T_{\rm top})/2$, is observed, Burnishev *et al.* [61] report a high-Rayleigh-number NOB convection with symmetric temperature profiles and a scaling $Nu \sim Ra^{\beta}$ which is comparable to the experiments in the OB limit at same Ra (see sect. 6). The data yield however a very strong dependence on the Prandtl number, most probably due to a strongly enhanced thermal expansion coefficient α.

For the second path as being relevant for liquids, strong NOB effects arise almost solely from a sensitive temperature dependence of material constants. Compressibility effects are subdominant and for corresponding experiments, we refer to [173] for glycerol and [174] for water. Following Gray and Giorgini [21], the linear temperature dependence of the mass density is then generalized to a polynomial of order M resulting to

$$\rho(T) = \rho_{\rm ref}\left[1 - \sum_{k=1}^{M} a_k (T - T_{\rm ref})^k\right], \qquad (65)$$

i.e., $a_1 = \alpha$, $a_k = 0$ for $k > 1$ refers to the OB case as given by eq. (6). Similarly one has to proceed for the other material parameters such as α, ν, k, and κ. The reference temperature is then the centre temperature $T_{\rm ref} = (T_{\rm bottom} + T_{\rm top})/2$. Numerically, the effect of such temperature dependence as given in (65) was studied in two-dimensional DNS with expansions up to $M = 5$ [75] and more recently in three-dimensional DNS up to $M = 7$ [175] for glycerol at $Pr \approx 2500$.

The understanding of the breaking of the up-down symmetry is in the focus of most studies on NOB convection. Several models have been suggested to understand the asymmetry of the centre temperature and thus the asymmetry of the boundary layers at the top and bottom better, *e.g.*, phenomenological models by Wu and Libchaber [171] or boundary layer models by Ahlers *et al.* [174].

In [174] it is found that the extension of the Prandtl-Blasius BL theory to NOB convection which uses $\nu(T)$ and $\kappa(T)$ in water agrees with the experiments. The approach worked however less well for cases with very strong temperature dependence of the material parameters such as for $\alpha(T)$ in ethane [60] or all material parameters in glycerol [175].

A different route was taken in DNS by Sameen *et al.* [176] at $Pr = 0.7$ and $Ra = 2 \times 10^8$ using the full set of compressible equations of motion. In this study, dependencies of the material parameters were implemented one at a time as monotonically increasing or decreasing functions with respect to T. Such procedure, which is possible only in numerical simulations, allows to disentangle the importance of different material parameters for the NOB effects on heat transport and the asymmetry of temperature profile. Monotonically decreasing $k(T)$ and $\alpha(T)$ diminish Nu while a monotonic nonlinear decrease of $\rho(T)$ increases Nu since the temperature feedback on the flow via the buoyancy term is amplified. The effect of $\nu(T)$ was however small.

This compact overview indicates one thing: the NOB effects depend very sensitively on the particular working fluid. Particular material parameters can dominate in one fluid, but are subdominant in another one. Clearly, we are still far away from a complete understanding of this variety of NOB effects.

7.2 Convection with phase changes

Atmospheric and many technological convection flows are associated with phase changes. Two topics have to be combined then which are already complicated in their own, the physics of turbulent flows and transport and the highly nonlinear thermodynamics of phase changes. Phase transitions are associated with latent heat releases during condensation or evaporative cooling —local sources and sinks of heat which drive additional local fluid motion. In the examples presented below phase changes will additionally break the up-down-symmetry in turbulent convection, thus introducing NOB-like effects into the convection flow. Experimentally, convection experiments with phase changes pose further challenges as the condensate is dominantly forming at the plates such as in the two-phase experiments with homogeneous nucleation [177].

7.2.1 Bubbly convection and boiling

In chemical and power engineering, boiling processes are of central interest. Boiling is accompanied by the formation of bubbles which can be described on different ways. In refs. [178,179], the impact of vapor bubbles on the heat transfer has been studied by modeling them as inertial point particles which can grow and shrink and act back thermally and mechanically on the flow. The effect of the bubbles on the flow depends on the Jacob number which relates sensible heat to the latent heat.

$$Ja = \frac{\rho_f c_p (T_{\rm hot} - T_{\rm sat})}{\rho_v L}\,, \qquad (66)$$

with the mass density of the liquid ρ_l and of the vapor ρ_v, the saturation temperature of the liquid $T_{\rm sat}$ and the latent heat L. The DNS that modeled the bubbles in the Lagrangian frame of reference showed that for small Jacob numbers the convection flow is stabilized. With increasing Ja the bubbles enhance the turbulent heat transport significantly. The breaking of the up-down symmetry of the convective heat flux and the bubble distribution across the cell was analyzed in [179], the impact of the vapor bubbles on the velocity fluctuations and the dissipation rates in [180].

An alternative route was taken by Biferale *et al.* [181] very recently. The application of the Lattice Boltzmann method allows to track bubbles as finite-size particles with deformations. The simulations confirmed the findings of the microbubble convection studies and demonstrated that the local latent heat release enhances the intermittency of the temperature fluctuations.

7.2.2 Moist convection and clouds formation

The most prominent example for moist convection is the formation of clouds in the atmosphere. Clouds are still the biggest source of uncertainty for more reliable climate prognoses [182]. A deeper physical understanding of cloud feedbacks can be achieved by reducing the complexity and disentangling different processes in order to quantify their importance and separate impact. This is done here by discussing some possible extensions of the classical (dry) Rayleigh-Bénard convection to moist convection case in the anelastic or OB regime which are given by eqs. (5) and (8), respectively. Moist convection requires to monitor the balances of vapor content, liquid water droplets (and even ice particles) beside the temperature. This set of equations is thus larger than the original OB equations. When warm clouds are discussed ice can be neglected and we are left with two components only, vapor and water.

The buoyancy B in atmospheric convection is given in its general form by [19]

$$B(T, q_v, q_l, p) = -g \frac{\rho(T, q_v, q_l, p) - \rho_{\rm ref}}{\rho_{\rm ref}}\,, \qquad (67)$$

with T being now the (potential) temperature and $q_v = \rho_v/\rho_{\rm dry}$, $q_l = \rho_l/\rho_{\rm dry}$ the mixing ratios of water vapor and liquid water, where $\rho_{\rm dry}$ is the mass density of dry air. Equation (67) is a generalized form that is added to the momentum equation. In single-phase convection it simplifies to $B = \alpha g(T - T_{\rm ref})$ as already given in eq. (7). Without rain, the liquid water and vapor are permanently converted into each other, but their sum, the so-called total water mixing ratio $q_t = q_v + q_l$, remains conserved. This can be used to simplify the model further. Several Boussinesq or anelastic models of moist convection have been discussed in recent years. The different levels of complexity are manifest in different levels of simplification for the buoyancy (67).

In the Boussinesq or anelastic moist Rayleigh-Bénard model [183–185] the (potential) temperature is substituted

by the equivalent (potential) temperature and the additional impact of the liquid water on the buoyancy of the air parcels is included. This results in

$$B(T, q_v, q_l) = g\left[\alpha(T - T_{\rm ref}) + \xi(q_v - q_{v,\rm ref}) - q_l\right], \quad (68)$$

where $\xi = R_v/R_d - 1$ with the gas constants for vapor and dry air, R_v and R_d [183]. The temperature equation (9) has to be extended by a latent heat release source term due to condensation of water. Furthermore, two additional scalar advection equations for q_v and q_l have to be added to the set of equations of motion. Additionally, a microphysical model is necessary that determines the condensation rate. Alternatively, Euler-Lagrangian models can be set up in which the water content is treated as an ensemble of inertial point-like droplets and the liquid water content is thus "discretized" [183].

If one limits the studies to the OB case, a further level of simplification can be obtained. We can simplify the equation of state $B(T, q_t)$ to a piecewise linear function of the state variables, T and q_t, at both sides of the phase boundary [186,187] at a given height z. This procedure still preserves the most important property, the discontinuity of the derivatives of the buoyancy with respect to the state variables. Potential temperature T and total water content q_t can afterwards be linearly recombined to two new buoyancy fields that represent, in a nutshell, the unsaturated vapor or the liquid water in the convection system. These are the dry and moist buoyancy field, D and M, which are given by

$$D = \left.\frac{\partial B}{\partial T}\right|_{q_t^{(u)},z}(T - T_{\rm ref}) + \left.\frac{\partial B}{\partial q_t}\right|_{T^{(u)},z}(q_t - q_{t,\rm ref}), \quad (69)$$

$$M = \left.\frac{\partial B}{\partial T}\right|_{q_t^{(s)},z}(T - T_{\rm ref}) + \left.\frac{\partial B}{\partial q_t}\right|_{T^{(s)},z}(q_t - q_{t,\rm ref}). \quad (70)$$

Due to the linearization all partial derivatives are constants, but of different magnitude for the unsaturated (u) and saturated (s) sides of the phase boundary. The saturation condition which determines if liquid water or unsaturated vapor is present follows by the explicit relation [187]

$$B(D, M, z) = \max(M, D - N_s^2 z), \quad (71)$$

where $N_s^2 = g(\Gamma_u - \Gamma_s)/T_{\rm ref}$ is the square of the Brunt-Vaisala frequency which contains the dry and moist adiabatic lapse rates, Γ_u and Γ_s. Equation (68) determines the saturation at each spatio-temporal point explicitly. The air parcel is saturated whenever $M > D - N_s^2 z$ [187].

Two advection diffusion equations for D and M have to be solved instead of a temperature equation in the dry OB case. There are now four equations of motion and the saturation condition (68) that describe the problem. The number of system parameters is five, a Prandtl number Pr, a dry and a moist Rayleigh number, Ra_D and Ra_M, and two parameters that prescribe the amount of liquid water (or a deficit) at the top and bottom plane. One can run this model in two fundamentally different states of turbulent moist convection: the linearly unstable regime [188] and the conditionally unstable regime [189]. These two regimes start from different equilibria and result in the two main regimes of low cloud formations —stratocumulus-type convection in the former and cumulus-type convection for the latter. They are illustrated in fig. 10. In the linearly unstable regime, both buoyancy fields are unstably stratified such as the temperature in the original OB case. Consequently, $Ra_D > 0$ and $Ra_M > 0$. In the conditionally unstable regime, unsaturated air is however stably stratified and thus $Ra_D < 0$ and $Ra_M > 0$. Convection patterns become then localized and isolated and do not fill the whole layer as seen in fig. 10 (right). Moist convection in the conditionally unstable regime has some parallels with wall-bounded shear flows, *e.g.* with respect to the transition to turbulence [190,191].

A further level of simplification is achieved if unsaturated and saturated air (with cloud droplets) are combined in a scalar mixture fraction field χ similar to reacting species in turbulent combustion. The buoyancy is now prescribed as a function $B(\chi)$ [192]. In this case, one equation for the scalar field χ has to be solved together with the momentum balance, *i.e.*, the mathematical structure is identical to our original set of OB equations (7)–(9). This model has been successfully used to study entrainment of clear warm air at the top of closed stratocumulus cloud layers in high-resolution DNS [192]. It also demonstrated that turbulent entrainment processes are eventually determined by molecular diffusion. Both approaches [187] and [192] show that cloud dynamics at different scales can be described successfully on the level of the Boussinesq approximation by means of simplified DNS models that avoid parametrizations of the turbulence. It is also clear that these models have their limits. With a view to atmospheric convection, radiative transfer —an important driver of cloud formation processes— was therefore recently included for both cases.

8 Outlook

Turbulent Rayleigh-Bénard convection is perhaps one of the best studied fundamental flows in fluid mechanics. It has been an important example to study flow stability, pattern formation processes, and to test various concepts of nonlinear dynamics. As a turbulent flow it contains shear flow dynamics, anisotropies, and coherent structure formation close to the walls and (nearly) isotropic turbulence in the bulk. The temperature is an active driver of the dynamics at the boundaries while it behaves closer to a passive scalar field in the bulk. The amount of specific details on this flow which have been collected in the past decade is impressive. At the end of this review we want to discuss a few open points which are to our view important for further progress.

1) We have seen that all the experimental studies for the largest accessible Rayleigh numbers seem still to depend on specific details of the setup such as material properties of the working fluid, side wall conditions, aspect ratios of the cells. This means that at very high Rayleigh number this system is extremely sensitive to boundary

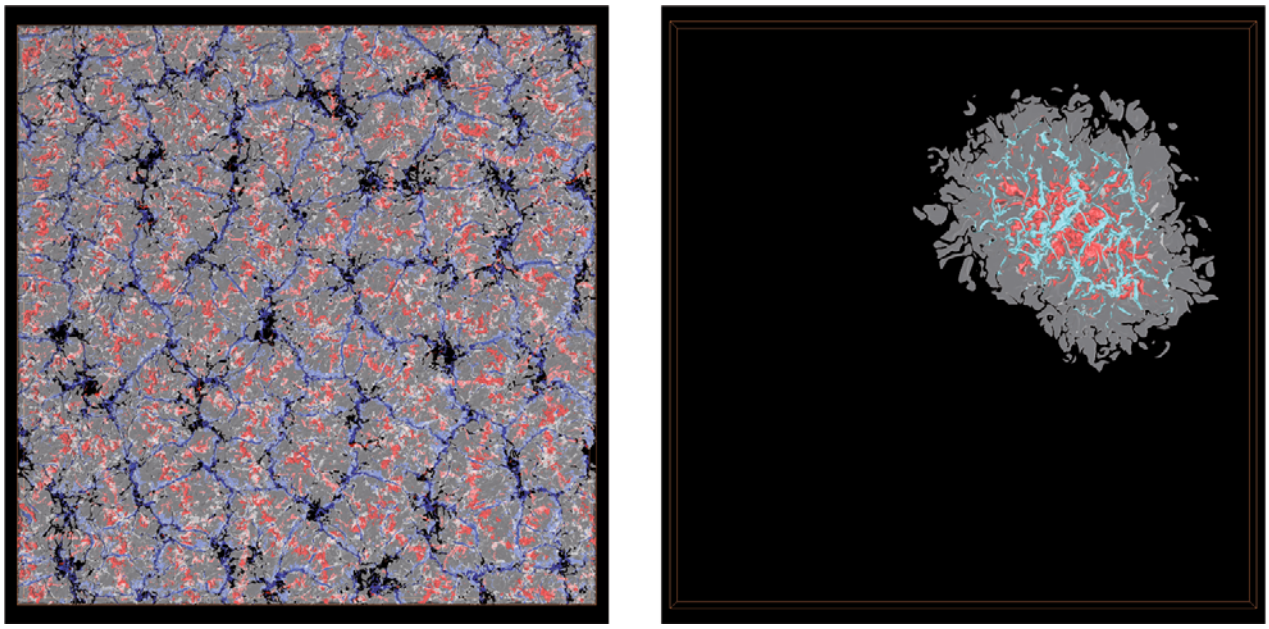

Fig. 10. View from the top onto a moist convection layer in two different regimes. Left: stratocumulus cloud-like regime in which dry and moist air is unstably stratified. Right: cumulus cloud-like regime in which the dry air is stably stratified and the moist air unstably stratified. The latter is also known as the conditionally unstable regime of convection. The blue isosurfaces denote strongly downwelling air, the red isosurfaces strongly upwelling air. The transparent gray isosurface shows the clouds. The DNS in the layer with an aspect ratio $\Gamma = 32$ is horizontally resolved with 4096 grid points and vertically with 129. The Rayleigh numbers are $Ra \lesssim 10^7$ in both cases (see [188,189] for details).

conditions. Side walls are not "innocent". But what is the ideal situation —an adiabatic or a conductive wall? There are certainly no side walls in atmospheric or solar convection to mention only two applications as stated in table 1. However, side wall effects are important in other applications such as indoor ventilation. Moreover, boundary conditions at the top and bottom of the atmosphere or in the Earth mantle can be a combination of prescribed fluxes and amplitudes. Two ways can be followed both in experiments and numerical simulations: try to avoid or diminish side boundaries effects and/or try to take all boundaries as precisely as possible into account. In the first case, it will be helpful to conduct more studies at higher aspect ratios —the only way to suppress the influences of side walls on the plume dynamics and the large-scale circulation. The second way is even more challenging (particularly from the theoretical point of view), but it is probably the only hope to understand the high-Rayleigh-number dynamics. We are aware of the fact that this puts additional challenges on experiment and DNS. Further complementary Lagrangian studies will be helpful here to understand the turbulent transport in this complex system.

2) The key to understand the transition to the ultimate regime of convection lies in the boundary layer dynamics. We are just beginning to unravel details of their complex behavior and dynamics as well as their interaction with the large scale flow. Our physical picture of the global turbulent transport is mostly based on highly idealized two-dimensional laminar boundary layer models for forced and natural convection. These models seem to work well when we compare the scaling of the boundary layer thicknesses *vs.* Ra with the measurements up to $Ra \sim 10^{12}$. One has to be however cautious if the idealized models are still reliable when it comes to understand the details of the transition to the turbulent state in the BL that is connected with the crossover to an ultimate regime of enhanced transport. Perhaps it is helpful here to study the active role of the temperature field in a boundary layer that is more complex than the classical models but less complex than the BL in a turbulent convection cell.

3) Recent parallels to another fundamental flow system, the turbulent Taylor-Couette flow between two concentric cylinders, can help to understand the ultimate regime in Rayleigh-Bénard convection better [193–196]. The reason for this hope is that the Taylor-Couette system seems to proceed to the ultimate state in a somehow more direct way since the shear flow is directly generated and not initiated via the buoyancy forces due to temperature differences.

4) It would be desirable to have further high-Rayleigh number studies at different Prandtl numbers such that the detailed interplay between the thermal and velocity boundary layer can be better understood.

5) As we have mentioned at the beginning, Rayleigh-Bénard convection is a simple paradigm for convection flows. In reality they are combined with other physical phenomena. Therefore we believe that extensions of Rayleigh-Bénard convection in the OB frame are necessary and helpful to understand the real flows. This does not mean that one has to jump immediately to the full level of complexity of such a convection problem, *e.g.* in the atmosphere or Sun. We think that it is useful to add complexity

incrementally, test out the limits of these new models, and to proceed afterwards to the next level. We could mention only a few examples and had to leave out many others, such as magnetoconvection or indoor ventilation. We are convinced that turbulent Rayleigh-Bénard convection will remain an exciting field for fundamental and applied fluid dynamics research in the next years.

We would like to thank all our colleagues and collaborators for their input and suggestions as well as many stimulating discussions on this exciting topic. JS acknowledges support by the Deutsche Forschungsgemeinschaft within the Research Group FOR 1182 and by the Jülich Supercomputing Centre (Germany) under grant HIL02.

References

1. F.H. Busse, Astrophys. J. **159**, 629 (1970).
2. R.J. Bray, R.E. Longhead, C.J. Durrant, *The Solar Granulation* (Cambridge University Press, Cambridge, 2009) pp. 276.
3. J.C. Wyngaard, Annu. Rev. Fluid Mech. **24**, 205 (1992).
4. B. Stevens, Annu. Rev. Earth Planet. Sci. **33**, 605 (2005).
5. S.A. Thorpe, Annu. Rev. Earth Planet. Sci. **32**, 91 (2004).
6. F.P. Incropera, *Liquid Cooling of Electronic Devices by Single-phase Convection* (John Wiley & Sons, New York, 1999) pp. 304.
7. R.J. Glicksman, Phys. Today **61**, 35 (2008).
8. C. Normand, Y. Pomeau, M.G. Velarde, Rev. Mod. Phys. **49**, 581 (1977).
9. U. Christensen, Annu. Rev. Earth Planet. Sci. **23**, 65 (1995).
10. B.A. Klinger, J. Marshall, Dyn. Atmos. Ocean **21**, 227 (1995).
11. B.W. Atkinson, J. Wu Zhang, Rev. Geophys. **34**, 403 (1996).
12. J. Christensen-Dalsgaard, D.O. Gough, M.J. Thompson, Astrophys. J. **378**, 413 (1991).
13. K.R. Sreenivasan, R.J. Donnelly, Adv. Appl. Mech. **37**, 239 (2001).
14. E.D. Siggia, Annu. Rev. Fluid Mech. **26**, 137 (1994).
15. S. Grossmann, D. Lohse, J. Fluid Mech. **402**, 27 (2000).
16. G. Ahlers, S. Grossmann, D. Lohse, Rev. Mod. Phys. **81**, 503 (2009).
17. D. Lohse, K.-Q. Xia, Annu. Rev. Fluid Mech. **42**, 335 (2010).
18. E. Bodenschatz, J. Schumacher (Editors), *Focus on New Perspectives in High-Rayleigh-Number Turbulent Convection*, New J. Phys., Vol. **12** (2011).
19. K.A. Emanuel, *Atmospheric Convection* (Oxford University Press, Oxford, 1994) pp. 580.
20. E.A. Spiegel, G. Veronis, Astrophys. J. **131**, 442 (1960).
21. D.D. Gray, A. Giorgini, Int. J. Heat Mass Transfer **19**, 545 (1976).
22. O. Pauluis, J. Atmos. Sci. **65**, 2719 (2008).
23. A. Oberdeck, Ann. Phys. (Leipzig) **243**, 271 (1879).
24. J. Boussinesq, *Theorie Analytique de la Chaleur*, Volume **II** (Gauthier-Villars, Paris, 1903) pp. 172–176.
25. D.J. Tritton, *Physical Fluid Dynamics* (Oxford University Press, Oxford, 1988) pp. 519.
26. M.S. Emran, J. Schumacher, J. Fluid Mech. **611**, 13 (2008).
27. J. Bailon-Cuba, M.S. Emran, J. Schumacher, J. Fluid Mech. **655**, 153 (2010).
28. W.V.R. Malkus, Proc. R. Soc. London, Ser. A **225**, 196 (1954).
29. W.V.R. Malkus, Proc. R. Soc. London, Ser. A **225**, 185 (1954).
30. B.I. Shraiman, E.D. Siggia, Phys. Rev. A **28**, 3650 (1990).
31. H. Schlichting, *Boundary Layer Theory* (McGraw Hill, New York, 1957) pp. 647.
32. S. Grossmann, D. Lohse, Phys. Rev. Lett. **86**, 3316 (2001).
33. S. Grossmann, D. Lohse, Phys. Rev. E **66**, 016305 (2002).
34. S. Grossmann, D. Lohse, Phys. Fluids **16**, 4462 (2004).
35. X.-D. Shang, X.-L. Qiu, P. Tong, K.-Q. Xia, Phys. Rev. Lett. **90**, 074501 (2003).
36. X.-D. Shang, P. Tong, K.-Q. Xia, Phys. Rev. Lett. **100**, 244503 (2008).
37. R. Lakkaraju, R.J.A.M. Stevens, R. Verzicco, S. Grossmann, A. Prosperetti, C. Sun, D. Lohse, submitted to Phys. Rev. E (2012).
38. R. H. Kraichnan, Phys. Fluids **5**, 1374 (1962).
39. C.H.B. Priestley, *Turbulent Transfer in the Lower Atmosphere* (Chicago University Press, Chicago, 1959) pp. 130.
40. L.N. Howard, J. Fluid Mech. **17**, 405 (1963).
41. F.H. Busse, J. Fluid Mech. **37**, 457 (1969).
42. C.R. Doering, P. Constantin, Phys. Rev. E **53**, 5957 (1996).
43. S. Grossmann, D. Lohse, Phys. Fluids **23**, 045108 (2011).
44. D. Funfschilling, E. Brown, A. Nikolaenko, G. Ahlers, J. Fluid Mech. **536**, 145 (2005).
45. A. Nikolaenko, E. Brown, D. Funfschilling, G. Ahlers, J. Fluid Mech. **523**, 251 (2005).
46. C. Sun, L.-Y. Ren, H. Song, K.-Q. Xia, J. Fluid Mech. **542**, 165 (2005).
47. F. Chillà, M. Rastello, S. Chaumat, B. Castaing, Eur. Phys. J. B **40**, 223 (2004).
48. J.-C. Tisserand, M. Creyssels, Y. Gasteuil, H. Pabiou, M. Gibert, B. Castaing, F. Chillà, Phys. Fluids **23**, 015105 (2011).
49. F. Chillà, S. Ciliberto, C. Innocenti, E. Pampaloni, Nuovo Cimento D **15**, 1229 (1993).
50. S. Ciliberto, S. Cioni, C. Laroche, Phys. Rev. E **54**, R5901 (1996).
51. Z.A. Daya, R.E. Ecke, Phys. Rev. Lett. **87**, 184501 (2001).
52. Y. Gasteuil, W.L. Shew, M. Gibert, F. Chillà, B. Castaing, J.-F. Pinton, Phys. Rev. Lett. **99**, 234302 (2007).
53. C. Sun, Y.-R. Cheung, K.-Q. Xia, J. Fluid Mech. **605**, 79 (2008).
54. B.A. Puthenveettil, G.S. Gunasegarane, Y.K. Agrawal, D. Schmeling, J. Bosbach, J.H. Arakeri, J. Fluid Mech. **685**, 335 (2011).
55. Y. Tsuji, T. Mizuno, T. Mashiko, M. Sano, Phys. Rev. Lett. **94**, 034501 (2005).
56. A. Belmonte, A. Tilgner, A. Libchaber, Phys. Rev. E **50**, 269 (1994).
57. A.S. Fleischer, R.J. Goldstein, J. Fluid Mech. **469**, 1 (2002).

58. G. Ahlers, D. Funfschilling, E. Bodenschatz, New J. Phys. **11**, 123001 (2009).
59. G. Ahlers, E. Bodenschatz, D. Funfschilling, J. Hogg, J. Fluid Mech. **641**, 157 (2009).
60. G. Ahlers, E. Calzavarini, F.F. Araujo, D. Funfschilling, S. Grossmann, D. Lohse, K. Sugiyama, Phys. Rev. E **77**, 046302 (2008).
61. Y. Burnishev, E. Segre, V. Steimberg, Phys. Fluids **22**, 035108 (2010).
62. X. He, D. Funfschilling, H. Nobach, E. Bodenschatz, G. Ahlers, Phys. Rev. Lett. **108**, 024502 (2012).
63. R. du Puits, C. Resagk, A. Tilgner, F.H. Busse, A. Thess, J. Fluid Mech. **572**, 231 (2007).
64. D.C. Threlfall, J. Fluid Mech. **67**, 17 (1975).
65. J.J. Niemela, L. Skrbek, K.R. Sreenivasan, R.J. Donelly, Nature **404**, 837 (2000).
66. R. Verzicco, P. Orlandi, J. Comput. Phys. **123**, 402 (1996).
67. R. Verzicco, R. Camussi, J. Fluid Mech. **477**, 19 (2003).
68. O. Shishkina, A. Shishkin, C. Wagner, J. Comput. Appl. Maths. **226**, 336 (2009).
69. P.F. Fischer, J. Comput. Phys. **133**, 84 (1997).
70. F. Hébert, R. Hufschmid, J. Scheel, G. Ahlers, Phys. Rev. E **81**, 046318 (2010).
71. M. Chandra, M.K. Verma, Phys. Rev. E **83**, 067303 (2011).
72. T. Hartlep, A. Tilgner, F.H. Busse, Phys. Rev. Lett. **91**, 064501 (2003).
73. J. Schumacher, Phys. Rev. Lett. **100**, 134502 (2008).
74. C. Wang, J.-G. Liu, H. Johnston, Num. Math. **97**, 555 (2004).
75. K. Sugiyama, E. Calzavarini, S. Grossmann, D. Lohse, Europhys. Lett. **80**, 34002 (2007).
76. G. Grötzbach, J. Comput. Phys. **49**, 241 (1983).
77. R.J.A.M. Stevens, R. Verzicco, D. Lohse, J. Fluid Mech. **643**, 495 (2010).
78. O. Shishkina, R.J.A.M. Stevens, S. Grossmann, D. Lohse, New J. Phys. **12**, 075022 (2010).
79. R.J.A.M. Stevens, D. Lohse, R. Verzicco, J. Fluid Mech. **688**, 31 (2011).
80. N. Shi, M.S. Emran, J. Schumacher, to be published in J. Fluid Mech., doi:10.1017/jfm.2012.207 (2012).
81. G. Ahlers, Phys. Rev. E **63**, 015303 (2001).
82. P.-E. Roche, B. Castaing, B. Chabaud, B. Hébral, J. Sommeria, Eur. Phys. J. B **24**, 015303 (2001).
83. R. Verzicco, Phys. Fluids **16**, 1965 (2004).
84. H.-D. Xi, S. Lam, K.-Q. Xia, J. Fluid Mech. **503**, 47 (2004).
85. H.-D. Xi, K.-Q. Xia, Phys. Fluids **20**, 055104 (2008).
86. S. Weiss, G. Ahlers, J. Fluid Mech. **676**, 5 (2011).
87. E.P. van der Poel, R.A.J.M. Stevens, D. Lohse, Phys. Rev. E **84**, 045303 (2011).
88. P.-E. Roche, B. Castaing, B. Chabaud, B. Hébral, Europhys. Lett. **58**, 693 (2002).
89. K.-Q. Xia, J. Fluid Mech. **676**, 1 (2011).
90. K.-Q. Xia, S.-L. Lui, Phys. Rev. Lett. **79**, 5006 (1997).
91. K.-Q. Xia, X.-L. Qiu, Europhys. Lett. **46**, 171 (1999).
92. P.-E. Roche, F. Gauthier, R. Kaiser, J. Salort, New J. Phys. **12**, 085014 (2010).
93. G. Ahlers, X. Xu, Phys. Rev. Lett. **86**, 3320 (2001).
94. X.-L. Qiu, P. Tong, Phys. Rev. Lett. **87**, 094501 (2001).
95. W.W. Spangenberg, W.R. Rowland, Phys. Fluids **4**, 743 (1961).
96. E.M. Sparrow, R. B. Husar, R.J. Goldstein, J. Fluid Mech. **41**, 793 (1970).
97. S.-Q. Zhou, K.-Q. Xia, Phys. Rev. Lett. **89**, 184502 (2002).
98. E.S.C. Ching, H. Guo, X.-D. Shang, P. Tong, K.-Q. Xia, Phys. Rev. Lett. **93**, 124501 (2004).
99. A. Belmonte, A. Libchaber, Phys. Rev. E **53**, 4893 (1996).
100. X. He, P. Tong, K.-Q. Xia, Phys. Rev. Lett. **98**, 144501 (2007).
101. O. Shishkina, C. Wagner, J. Fluid Mech. **546**, 51 (2006).
102. O. Shishkina, C. Wagner, J. Fluid Mech. **599**, 383 (2008).
103. Q. Zhou, C. Sun, K.-Q. Xia, Phys. Rev. Lett. **98**, 074501 (2007).
104. Q. Zhou, K.-Q. Xia, New J. Phys. **12**, 075006 (2010).
105. B.A. Puthenveettil, J.H. Arakeri, J. Fluid Mech. **542**, 217 (2005).
106. J. Schumacher, Phys. Rev. E **79**, 056301 (2009).
107. G. Zocchi, E. Moses, A. Libchaber, Physica A **166**, 387 (1990).
108. T. Haramina, A. Tilgner, Phys. Rev. E **69**, 056306 (2004).
109. F. Waleffe, Phys. Fluids **9**, 883 (1997).
110. C. Sun, K.-Q. Xia, P. Tong, Phys. Rev. E **72**, 026302 (2005).
111. C. Sun, H.-D. Xi, K.-Q. Xia, Phys. Rev. Lett. **95**, 074502 (2005).
112. S. Wagner, O. Shishkina, C. Wagner, J. Fluid Mech. **697**, 336 (2012).
113. C. Resagk, R. du Puits, A. Thess, F.V. Dolzhansky, S. Grossmann, F.F. Araujo, D. Lohse, Phys. Fluids **18**, 095105 (2006).
114. K.R. Sreenivasan, A. Bershadskii, J.J. Niemela, Phys. Rev. E **65**, 056306 (2002).
115. F.F. Araujo, S. Grossmann, D. Lohse, Phys. Rev. Lett. **95**, 084502 (2005).
116. E. Brown, G. Ahlers, J. Fluid Mech. **568**, 351 (2006).
117. M. Assaf, L. Angheluta, N. Goldenfeld, Phys. Rev. Lett. **107**, 044502 (2011).
118. K. Petschel, M. Wilczek, M. Breuer, R. Friedrich, U. Hansen, Phys. Rev. E **84**, 026309 (2011).
119. P.K. Mishra, A.K. De, M.K. Verma, V. Eswaran, J. Fluid Mech. **668**, 480 (2011).
120. Y.-B. Xin, K.-Q. Xia, P. Tong, Phys. Rev. Lett. **77**, 1266 (1996).
121. R.J. Adrian, Int. J. Heat Mass Transfer **39**, 2303 (1996).
122. K. Stewartson, Zeit. Angew. Math. Phys. **9**, 276 (1958).
123. Z. Rotem, L. Claassen, J. Fluid Mech. **39**, 173 (1969).
124. S.A. Theerthan, J.H. Arakeri, J. Fluid Mech. **373**, 221 (1998).
125. E.M. Sparrow, W.J. Minkowycz, Int. J. Heat Mass Transfer **5**, 503 (1962).
126. C.A. Hieber, Int. J. Heat Mass Transfer **16**, 769 (1973).
127. R. du Puits, C. Resagk, A. Thess, Phys. Rev. Lett. **99**, 234504 (2007).
128. Q. Zhou, K.-Q. Xia, Phys. Rev. Lett. **104**, 104301 (2010).
129. Q. Zhou, R.J.A.M. Stevens, K. Sugiyama, S. Grossmann, D. Lohse, K.-Q. Xia, J. Fluid Mech. **664**, 297 (2010).
130. M. van Reeuwijk, H.J.J. Jonker, K. Hanjalić, Phys. Rev. E **77**, 036312 (2008).
131. Q. Zhou, K. Sugiyama, R.J.A.M. Stevens, S. Grossmann, D. Lohse, K.-Q Xia, Phys. Fluids **23**, 125104 (2011).
132. S. Lam, X.-D. Shang, S.-Q. Zhou, K.-Q. Xia, Phys. Rev. E **65**, 066306 (2002).
133. S.-L. Lui, K.-Q. Xia, Phys. Rev. E **57**, 5494 (1998).

134. X.-L. Qiu, K.-Q. Xia, Phys. Rev. E **58**, 5816 (1998).
135. R.J.A.M. Stevens, Q. Zhou, S. Grossmann, R. Verzicco, K.-Q. Xia, D. Lohse, Phys. Rev. E **85**, 027301 (2012).
136. G. Ahlers, E. Bodenschatz, D. Funfschilling, S. Grossmann, X. He, D. Lohse, R.J.A.M. Stevens, R. Verzicco, submitted to Phys. Rev. Lett. (2012) arXiv:1204.6465.
137. Y.-B. Du, P. Tong, J. Fluid Mech. **407**, 57 (2000).
138. P.E. Roche, B. Castaing, B. Chabaud, B. Hebral, Phys. Rev. E **63**, 045303 (2001).
139. X.-L. Qiu, K.-Q. Xia, P. Tong, J. Turb. **6**, 2 (2005).
140. O. Shiskina, C. Wagner, J. Fluid Mech. **686**, 568 (2011).
141. D. Lohse, F. Toschi, Phys. Rev. Lett. **90**, 34502 (2003).
142. E. Calzavarini, C. R. Doering, J.D. Gibbon, D. Lohse, A. Tanabe, F. Toschi, Phys. Rev. E **73**, 035301(R) (2006).
143. M.R. Cholemari, J.H. Arakeri, Int. J. Heat Mass Transfer **48**, 4467 (2005).
144. M.R. Cholemari, J.H. Arakeri, J. Fluid Mech. **621**, 69 (2009).
145. M. Gibert, H. Pabiou, F. Chillà, B. Castaing, Phys. Rev. Lett. **96**, 084501 (2006).
146. M. Gibert, H. Pabiou, J.-C. Tisserand, B. Gertjerenken, B. Castaing, F. Chillà, Phys. Fluids **21**, 035109 (2009).
147. J.-C. Tisserand, M. Creyssels, M. Gibert, B. Castaing, F. Chillà, New J. Phys. **12**, 075024 (2010).
148. F. Perrier, P. Morat, J.L. Le Mouel, Phys. Rev. Lett. **89**, 134501 (2002).
149. L. E. Schmidt, E. Calzavarini, D. Lohse, F. Toschi, R. Verzicco, J. Fluid Mech. **691**, 52 (2012).
150. F. Toschi, E. Bodenschatz, Annu. Rev. Fluid Mech. **43**, 375 (2009).
151. W.L. Shew, Y. Gasteuil, M. Gibert, P. Metz, J.-F. Pinton, Rev. Sci. Instrum. **78**, 065105 (2007).
152. R. Ni, S.-D. Huang, K.-Q. Xia, J. Fluid Mech. **692**, 395 (2012).
153. W. Heisenberg, Z. Phys. **124**, 628 (1948).
154. A.M. Yaglom, Dokl. Akad. Nauk. SSSR **67**, 795 (1949).
155. G. Boffetta, I.M. Sokolov, Phys. Rev. Lett. **88**, 094501 (2002).
156. M.S. Emran, J. Schumacher, Phys. Rev. E **82**, 016303 (2010).
157. B. Castaing, G. Gunaratne, F. Heslot, L.P. Kadanoff, A. Libchaber, S. Thomae, X.Z. Wu, S. Zaleski, G. Zanetti, J. Fluid Mech. **204**, 1 (1989).
158. X.Z. Wu, A. Libchaber, Phys. Rev. A **45**, 842 (1992).
159. X. Chavanne, F. Chillà, B. Castaing, B. Hébral, B. Chabaud, J. Chaussy, Phys. Rev. Lett. **79**, 3648 (1997).
160. X. Chavanne, F. Chillà, B. Chabaud, B. Castaing, B. Hébral, Phys. Fluids **13**, 1300 (2001).
161. J.J. Niemela, K.R. Sreenivasan, J. Low Temp. Phys. **143**, 163 (2006).
162. J.J. Niemela, K.R. Sreenivasan, J. Fluid Mech. **481**, 355 (2003).
163. J.J. Niemela, K.R. Sreenivasan, J. Fluid Mech. **557**, 411 (2006).
164. J.J. Niemela, K.R. Sreenivasan, New J. Phys. **12**, 115002 (2010).
165. P.-P- Cortet, A. Chiffaudel, F. Daviaud, B. Dubrulle, Phys. Rev. Lett. **105**, 214501 (2010).
166. P.-E. Roche, F. Gauthier, B. Chabaud, B. Hébral, Phys. Fluids **17**, 115107 (2005).
167. F. Gauthier, P.-E. Roche, EPL **83**, 24005 (2008).
168. J.H. Preston, J. Fluid Mech. **3**, 373 (1958).
169. L.D. Landau, E.M. Lifschitz, *Course of Theoretical Physics: Fluid Mechanics* (Butterworth Heinemann, Oxford, 1987) pp. 539.
170. P. Urban, V. Musilova, L. Skrbek, Phys. Rev. Lett. **107**, 014302 (2011).
171. X.Z. Wu, A. Libchaber, Phys. Rev. A **43**, 2833 (1991).
172. G. Ahlers, F.F. Araujo, D. Funfschilling, S. Grossmann, D. Lohse, Phys. Rev. Lett. **98**, 054501 (2007).
173. J. Zhang, A. Libchaber, S. Childress, Phys. Fluids **10**, 1534 (1998).
174. G. Ahlers, E. Brown, F.F. Araujo, D. Funfschilling, S. Grossmann, D. Lohse, J. Fluid Mech. **569**, 409 (2006).
175. S. Horn, O. Shishkina, C. Wagner, J. Fluid Mech. (2012) submitted.
176. A. Sameen, R. Verzicco, K.R. Sreenivasan, EPL **86**, 14006 (2009).
177. J.-Q. Zhong, D. Funfschilling, G. Ahlers, Phys. Rev. Lett. **102**, 124501 (2009).
178. P. Oresta, R. Verzicco, D. Lohse, A. Prosperetti, Phys. Rev. E **80**, 026304 (2009).
179. L.E. Schmidt, P. Oresta, F. Toschi, R. Verzicco, D. Lohse, A. Prosperetti, New J. Phys. **13**, 025002 (2011).
180. R. Lakkaraju, L.E. Schmidt, P. Oresta, F. Toschi, R. Verzicco, D. Lohse, A. Prosperetti, Phys. Rev. E **84**, 036312 (2011).
181. L. Biferale, P. Perlekar, M. Sbragaglia, F. Toschi, Phys. Rev. Lett. **108**, 104502 (2012).
182. E. Bodenschatz, S.P. Malinowski, R.A. Shaw, F. Stratmann, Science **327**, 970 (2010).
183. P.A. Vaillancourt, M.K. Yau, W.W. Grabowski, J. Atmos. Sci. **58**, 1945 (2001).
184. M. Andrejczuk, W.W. Grabowski, S.P. Malinowski, P.K. Smolarkiewicz, J. Atmos. Sci. **61**, 1726 (2004).
185. K. Spyksma, P. Bartello, M.K. Yau, J. Turb. **7**, 32 (2006).
186. C.S. Bretherton, J. Atmos. Sci. **44**, 1809 (1987).
187. O. Pauluis, J. Schumacher, Comm. Math. Sci. **8**, 295 (2010).
188. T. Weidauer, O. Pauluis, J. Schumacher, New J. Phys. **12**, 105002 (2010).
189. O. Pauluis, J. Schumacher, Proc. Natl. Acad. Sci. U.S.A. **108**, 12623 (2011).
190. B. Eckhardt, T.M. Schneider, B. Hof, J. Westerweel, Annu. Rev. Fluid Mech. **39**, 447 (2007).
191. T. Weidauer, O. Pauluis, J. Schumacher, Phys. Rev. E **84**, 046303 (2011).
192. J.P. Mellado, J. Fluid Mech. **660**, 5 (2010).
193. B. Eckhardt, S. Grossmann, D. Lohse, J. Fluid Mech. **581**, 221 (2007).
194. M.S. Paoletti, D.P. Lathrop, Phys. Rev. Lett. **106**, 024501 (2011).
195. D.P.M. van Gils, S.G. Huisman, G.-W. Bruggert, C. Sun, D. Lohse, Phys. Rev. Lett. **106**, 024502 (2011).
196. S.G. Huisman, D.P.M. van Gils, S. Grossmann, C. Sun, D. Lohse, Phys. Rev. Lett. **108**, 024501 (2012).